Biomedicine & Pharmacotherapy 192 (2025) 118579

Contents lists available at ScienceDirect

Biomedicine & Pharmacotherapy

journal homepage: www.elsevier.com/locate/biopha

Tumor-targeted delivery of CXCL10 by mesenchymal stromal cells potentiates adoptive T cell therapy to treat solid tumors

Jeong Ho Yoon [a,1], Gyu-Bum Yeon [a,b,1], Hojae Lee [a], Hyunseo An [a], Jiwon Oh [a], Seok-Jin Kang [a], In-Byung Park [a], Seon Ah Lim [c], Soo Seok Hwang [d,e], Dae-Sung Kim [a,b,f], Ji Hyung Kim [a], Taehoon Chun [a], Yang-Xin Fu [g], Joonbeom Bae [a,*]

[a] Department of Biotechnology, College of Life Sciences and Biotechnology, Korea University, Seoul 02841, Republic of Korea
[b] Institute of Animal Molecular Biotechnology, Korea University, Seoul 02841, Republic of Korea
[c] Department of Life Science, Ewha Womans University, Seoul 03760, Republic of Korea
[d] School of Biological Sciences, Seoul National University, Gwanak-ro 1, Seoul 08826, Republic of Korea
[e] Institute of Molecular Biology and Genetics, Seoul National University, Gwanak-ro 1, Seoul 08826, Republic of Korea
[f] Department of Pediatrics, Korea University College of Medicine, Guro Hospital, Seoul 08308, Republic of Korea
[g] Department of Basic Medical Sciences, School of Medicine, Tsinghua University, Beijing 100084, China

ARTICLE INFO

Keywords:
Mesenchymal stromal cell (MSCs)
Cancer immunotherapy
Cell therapy
Chemotaxis
CXCL10
Adoptive T cell therapy (ACT)

ABSTRACT

Limited T cell infiltration into solid tumors remains one of the major obstacles to successful cancer immunotherapy, particularly for adoptive cell therapy (ACT). Although the chemokine CXCL10 recruits T cells, its direct therapeutic application is hampered by poor pharmacokinetics, systemic leakage, and failure to establish stable concentration gradients required for effective cell migration. To overcome these challenges, we engineered mesenchymal stromal cells (MSCs) to co-express NAD(P)H quinone oxidoreductase 1 (NQO1) for enhanced survival and CXCL10-Fc fusion protein for sustained chemokine delivery (NIP-MSCs). The engineered MSCs exhibited resilience to tumor microenvironment conditions through improved redox homeostasis, resulting in enhanced persistence and sustained IP10-Fc production *in vivo*. Crucially, tumor-targeted delivery of CXCL10-Fc established potent chemotactic gradients with minimal systemic leakage, dramatically increasing both endogenous and adoptively transferred T cell recruitment to tumor site. In syngeneic mouse models, NIP-MSC treatment significantly suppressed tumor growth through enhanced $CD8^+$ T cell infiltration. When combined with ACT in melanoma models, NIP-MSCs resulted in superior tumor control and significantly prolonged survival compared to conventional approaches. This work validates NIP-MSCs as a promising platform to overcome T cell exclusion and potentiate immunotherapy efficacy in solid tumors.

1. Introduction

Cancer immunotherapy has fundamentally transformed oncology by leveraging the innate capacity of immune system to eradicate malignant cells. The clinical success of immune checkpoint blockade (ICB) therapies targeting PD-1/PD-L1 and CTLA-4 pathways, alongside the promising outcomes from various adoptive cell transfer (ACT) approaches, has definitively established the enormous therapeutic potential of harnessing anti-tumor immunity [1]. However, effective tumor destruction requires robust effector T cell infiltration into the tumor microenvironment (TME), yet this remains a critical barrier limiting the efficacy of many immunotherapies [2,3]. Indeed, the abundance and distribution of tumor-infiltrating lymphocytes (TILs) are potent prognostic markers across diverse cancers, highlighting T cell recruitment into the tumor site as a pivotal determinant of therapeutic success [4,5].

The trafficking of T cells into TME is a tightly regulated process orchestrated by chemokines and their receptors [6]. The C-X-C motif chemokine receptor 3 (CXCR3) and its ligand axis is particularly vital for guiding cytotoxic T lymphocytes into solid tumors [7]. CXCR3, expressed predominantly on activated T and NK cells, binds three IFNγ-inducible chemokines: C-X-C motif chemokine ligand 9 (CXCL9), CXCL10 (also known as interferon-gamma-induced protein 10, IP-10),

* Corresponding author.
E-mail address: Joonbeombae@korea.ac.kr (J. Bae).
[1] These authors contributed equally to this work.

https://doi.org/10.1016/j.biopha.2025.118579

Available online 20 September 2025
0753-3322/© 2025 The Author(s). Published by Elsevier Masson SAS. This is an open access article under the CC BY license (http://creativecommons.org/licenses/by/4.0/).

and CXCL11 [8]. Among the CXCR3 ligands, each chemokine exhibits distinct expression patterns and functional characteristics that influence their therapeutic potential. CXCL9 shows more restricted cellular sources, primarily from immune cells [9,10], which could theoretically provide more precise spatial control through sharper concentration gradients. CXCL11, while having high receptor binding affinity, is functionally absent in C57BL/6 mice commonly used in cancer research [11,12], limiting its experimental utility. CXCL10 displays broader expression across multiple cell types and maintains consistent activity across experimental models, making it an attractive therapeutic candidate [13–15]. However, this widespread expression pattern presents a paradoxical challenge for therapeutic applications. The same broad production that makes CXCL10 readily available could potentially dilute the concentration gradients essential for effective chemotaxis, and conventional protein administration approaches further compound this problem by failing to establish and maintain the precise concentration gradients necessary for directed cell migration [16,17]. Substantial systemic leakage of administered proteins from the tumor site disrupts localized concentration gradients and may lead to off-target effects [18]. Additionally, CXCL10 exhibits susceptibility to rapid degradation through proteolytic processes and enzymatic inactivation [19,20]. These biological hurdles necessitate novel approaches to maintain functional, tumor-localized chemokine gradients while minimizing systemic distribution.

To overcome these limitations, cell-based delivery systems offer an engrossing strategy for sustained, localized production of chemokines within the TME [21,22]. Mesenchymal stromal cells (MSCs) are particularly attractive vehicles due to their tumor-tropism capacity [23,24], amenability to genetic engineering [25,26], and well-documented safety in clinical settings [27,28]. Engineered MSCs have already demonstrated promise in delivering various anti-cancer agents, including cytokines and ICB, directly to the tumor site [29,30]. However, the therapeutic utility of MSCs is often compromised by hostile TME, characterized by hypoxia, nutrient scarcity, oxidative stress, and chronic inflammation [31,32]. Poor survival and persistence of administered MSCs curtail their therapeutic output and often necessitate repeated dosing, escalating treatment complexity and cost. Consequently, strategies to bolster MSC resilience within this challenging environment are paramount for enhancing their efficacy as therapeutic delivery platforms.

NAD(P)H quinone oxidoreductase 1 (NQO1), a cytoprotective enzyme that detoxifies quinones via two-electron reduction and prevents the generation of damaging reactive semiquinone intermediates, has emerged as a key factor in cellular stress resistance [33]. NQO1 is integral to maintaining cellular redox balance, modulating NAD^+/NADH ratios, and protecting against oxidative damage, thereby influencing multiple cell survival pathways [34,35]. Indeed, NQO1 upregulation correlates with enhanced resistance to stressors prevalent in the TME, such as hypoxia and nutrient deprivation [36,37].

This study was predicated on the hypothesis that engineering MSCs to co-express NQO1 and a stabilized IP10-Fc fusion protein would confer superior anti-tumor effects. We hypothesized that this engineered cellular platform would provide dual therapeutic benefits: the NQO1-mediated enhancement of MSC survival within the harsh TME would ensure sustained local IP10-Fc production, while the continuous secretion of IP10-Fc would establish physiologically relevant chemotactic gradients for optimal recruitment of tumor-reactive T cells. Here, we demonstrate that these NQO1 enhanced, IP10-Fc-secreting MSCs (NIP-MSCs) significantly enhanced T cell infiltration into tumor site and significantly increase the efficacy of ACT in murine cancer models. These findings highlight the NIP-MSC as a potent adjunctive strategy to augment current cancer immunotherapies.

2. Results

2.1. High CXCL10 expression correlates with improved patient survival and T cell infiltration

To establish the clinical relevance of *CXCL10* as a therapeutic target, we analyzed the relationship between *CXCL10* expression and patient outcomes using clinical data from The Cancer Genome Atlas (TCGA). The analysis revealed that higher *CXCL10* expression was significantly associated with improved survival outcomes. In the pan-cancer analysis, patients with high *CXCL10* expression demonstrated markedly prolonged overall survival compared to those with low expression (HR = 0.55, 95 % CI: 0.46–0.65, logrank P = 8.7e-12) (Fig. 1A, left panel). A significant positive correlation between *CXCL10* expression and overall survival is also observed in melanoma patients (HR = 0.65, 95 % CI: 0.49–0.85, logrank P = 0.0014) (Fig. 1A, right panel). The survival benefit of high *CXCL10* expression extended to progression-free survival in both the pan-cancer cohort (HR = 0.48, 95 % CI: 0.39–0.61, logrank P = 6.7e-11) and melanoma patients (HR = 0.44, 95 % CI: 0.32–0.6, logrank P = 1.2e-07) (Fig. 1B). Further investigation using multiple computational deconvolution methods, including xCELL, TIMER, quanTIseq, MCP-counter, CIBERSORT-ABS, and CIBERSORT [38], demonstrated that *CXCL10* expression positively correlated with $CD8^+$ T cell infiltration across multiple cancer types (Fig. 1C). The correlation was particularly strong for effector and memory $CD8^+$ T cells, while naive T cells showed comparatively lower correlation, suggesting that *CXCL10* plays an important role in recruiting cytotoxic T lymphocytes to the TME.

2.2. Intratumorally administered Cxcl10 exhibits systemic leakage and fails to generate concentration gradient

Based on the observed correlation between *CXCL10* expression and T cell infiltration, we hypothesized that exogenously administered CXCL10 could enhance $CD8^+$ T cell recruitment and subsequently improve antitumor immunity. However, a significant challenge with native CXCL10 is its short biological half-life and rapid clearance from circulation, typical of small chemokine proteins [15,19]. To overcome these pharmacokinetic limitations and extend protein stability for sustained therapeutic effect, we engineered a fusion protein (recombinant mouse IP10-Fc, IP10-Fc) consisting of mouse CXCL10 fused with a human IgG Fc domain (Fig. S1A) [39,40]. We administered this fusion protein intratumorally into MC38 tumor-bearing mice to evaluate its biodistribution pattern following injection (Fig. 1D). After intratumoral (i.t.) administration of IP10-Fc, significant amount of fusion protein was detected in serum (2.41 ± 0.16 μg/mL) (Fig. 1E). Additionally, substantial leakage of the IP10-Fc was observed in various organs including lung, liver, heart, kidney, and spleen, with concentrations in these organs (0.66 ± 0.08 ng/mg, 0.37 ± 0.03 ng/mg, 0.71 ± 0.06 ng/mg, 0.70 ± 0.10 ng/mg, and 0.63 ± 0.11 ng/mg, respectively) exceeding those measured in the tumor tissue itself (0.32 ± 0.08 ng/mg) (Fig. 1F). Since the biological activity of chemokines such as CXCL10 fundamentally depends on maintaining concentration gradients to orchestrate directional cell migration [41], these findings highlight the critical need for a localized delivery system that can minimize systemic leakage and maintain effective chemokine gradients within the TME.

2.3. Enhanced NQO1 expression improves MSC survival under stress conditions by maintaining cellular redox homeostasis

MSCs are encouraging delivery vehicles for the delivery of IP10-Fc due to their amenability to genetic engineering and natural tropism for tumor sites [28]. As a living vehicle, increasing the persistence of MSCs under harsh conditions such as TME represents a promising strategy to enhance the production of therapeutics and prolong the therapeutic effect. To improve the persistence of MSCs within the TME,

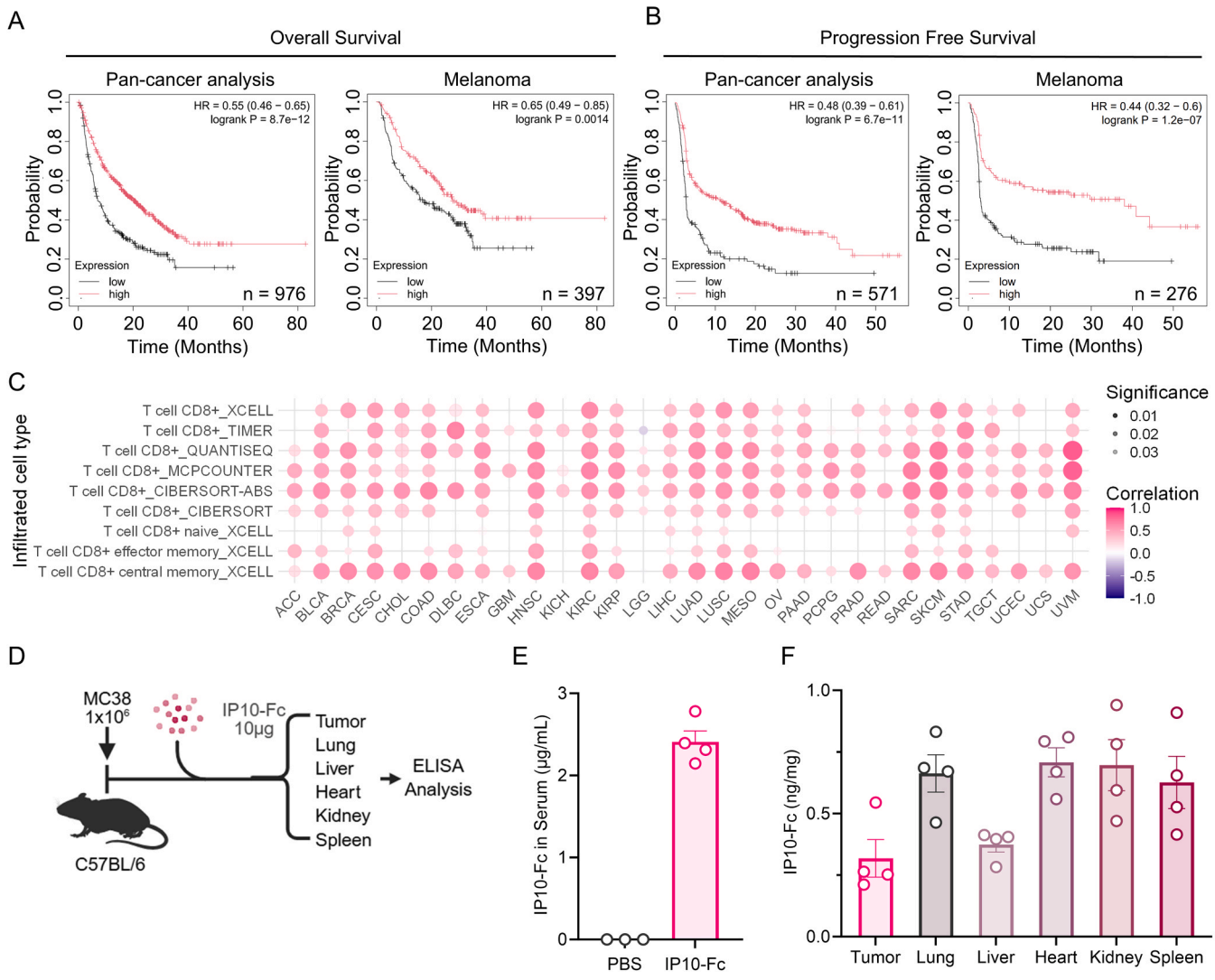


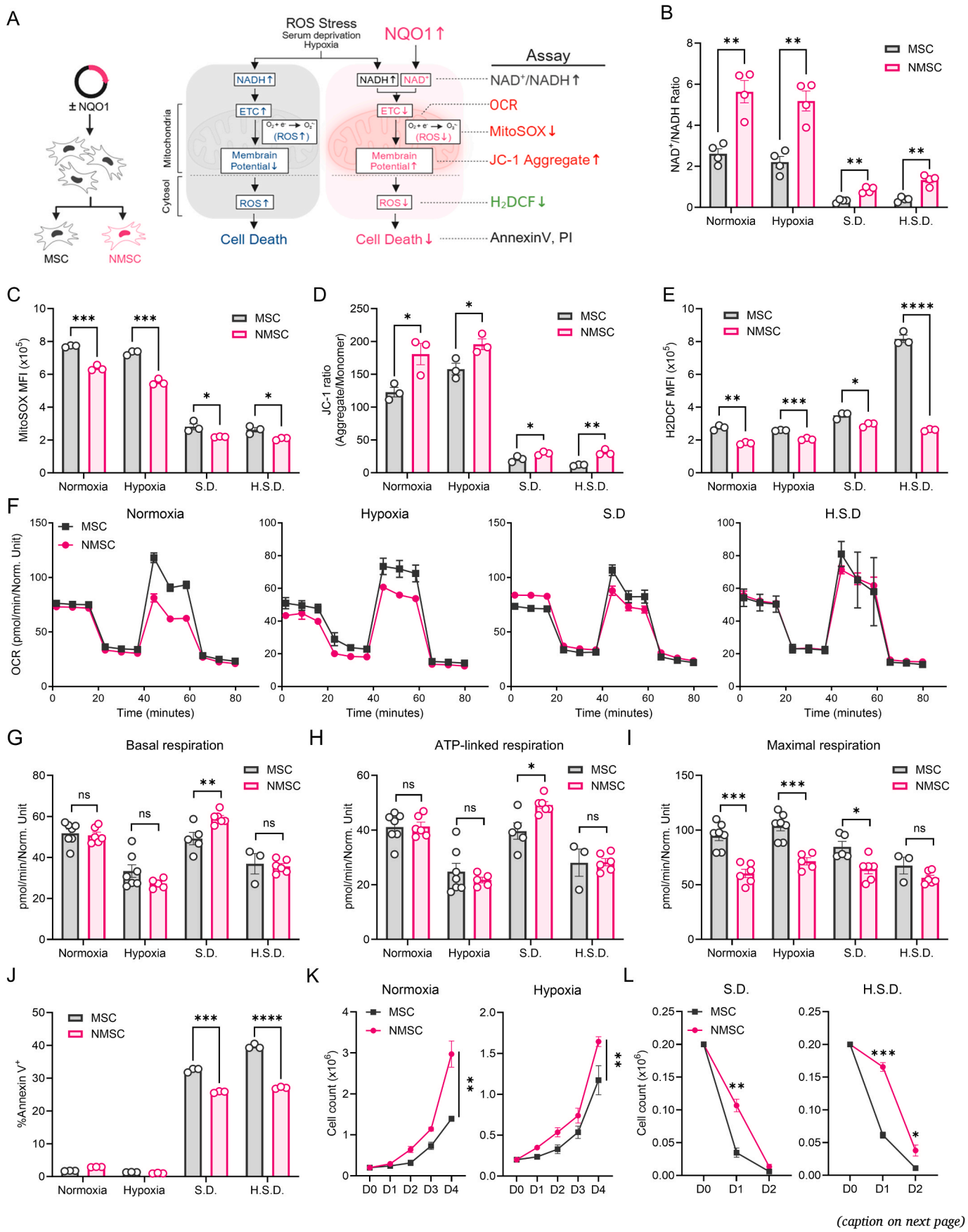
Fig. 1. Prognostic value of CXCL10 and systemic leakage of intratumorally administered IP10-Fc. (A and B) Kaplan-Meier plots of overall survival (A) and progression-free survival (B) based on CXCL10 expression levels. Left panels show pan-cancer analysis; right panels show melanoma patients specifically. Patients were stratified into high and low CXCL10 expression groups. (C) Correlation matrix between CXCL10 expression and $CD8^+$ T cell infiltration across multiple cancer types, retrieved from TIMER 2.0 (D) Schematic of intratumoral IP10-Fc biodistribution experiment in MC38 tumor-bearing mice. (E and F) C57BL/6 mice (n = 5) were s.c. inoculated with 1×10^6 MC38 cells; 10 days after tumor inoculation, 20 μg IP10-Fc was i.t. injected. 6 h after administration, serum concentration (E) and tissue biodistribution (F) of IP10-Fc were determined by ELISA. Data are shown as mean ± s.e.m. from two to three independent experiments. *P* value was determined by long-rank test (A and B). The diagram in (D) was created using BioRender. Ku, G. (2025) https://BioRender.com/2ufys7l.

MSCs were transduced to express NQO1 (NMSC), a protective enzyme that catalyzes the NAD(P)H-dependent reduction of quinones to hydroquinones while preventing formation of reactive semiquinone radicals, and confers resistance to stress-induced apoptosis [42,43] (Fig. S1B).

To evaluate the effect of NQO1 on cell persistence under stress conditions, cells were cultured under TME-mimicking conditions and sequentially examined for cellular redox state, mitochondrial membrane potential, and apoptosis (Fig. 2A). Beginning with the primary effect of NQO1 on cellular redox state, we observed a substantially increased level of NAD^+/NADH ratio in cells under stressful conditions (Fig. 2B). This favorable shift in redox balance directly impacted electron transport chain function, as evidenced by reduced mitochondrial-specific ROS measured by mitoSOX across all cell culture conditions (Fig. 2C). Mitochondrial membrane integrity was thereby preserved, with the NMSCs showing significantly enhanced membrane potential in JC-1 staining (Fig. 2D). Consequently, NMSCs showed markedly reduced cellular oxidative stress, with H2DCFDA measurements revealing significantly lower cytosolic ROS levels compared to controls, especially under severe combined stress conditions (Fig. 2E).

To gain deeper mechanistic insights into the improved mitochondrial function, we measured oxygen consumption rate (OCR) across all stress conditions (Fig. 2F). The results revealed a distinct condition-specific metabolic profile in NMSCs. While maximal respiratory capacity was consistently reduced in NMSCs across all tested conditions, basal respiration and ATP-linked respiration remained comparable to control MSCs under most environments (Fig. 2G-I). Most notably, serum deprivation conditions uniquely enhanced both basal and ATP-linked respiration in NMSCs compared to control MSCs, while combined hypoxia and serum deprivation normalized all parameters to control levels.

According to established respirometry guidelines, the pattern of selectively reduced maximal respiration may indicate altered substrate utilization capacity, potentially related to competitive NADH utilization by overexpressed NQO1 [44,45]. However, the maintained basal respiratory function combined with enhanced respiration specifically under nutrient limitation suggests adaptive metabolic flexibility rather than mitochondrial dysfunction. Under serum deprivation, the enhanced NAD^+ regeneration capacity of NQO1 may facilitate increased



(caption on next page)

Fig. 2. NQO1 enhances MSC survival under stress conditions. (A) Schematic depicting NQO1-mediated cytoprotection mechanisms against ROS stress. (B to E) BM-MSCs and NMSCs were cultured under normoxia, hypoxia, serum deprivation (S.D.), or combined hypoxia and serum deprivation (H.S.D.) for 6 h (n = 3). Cellular stress responses were evaluated by measuring (B) NAD^+/NADH ratio, (C) mitochondrial ROS levels using MitoSOX, (D) mitochondrial membrane potential using JC-1, (E) cytosolic ROS levels using H2DCFDA. (F-I) Cells were cultured under normoxia, hypoxia, S.D., or H.S.D. for 24 h. Oxygen Consumption Rate (OCR) of MSCs and NMSCs measured by Seahorse XF Pro Analyzer (F). Key parameters derived from the OCR result; basal respiration (G), ATP-linked respiration (H) and maximal respiration (I). (J) Apoptotic profiles using Annexin V/PI staining on cells incubated under normoxia, hypoxia, serum deprivation (S.D.), or combined hypoxia and serum deprivation (H.S.D.) for 6 h (n = 3). (K and L) Growth curves of MSCs and NMSCs under stress conditions. 2.0×10^5 cells were seeded initially and counted every 24 h (n = 3). Cells were cultured under normoxia or hypoxia (K), and S.D. or H.S.D. conditions (L). Data are shown as mean ± s.e.m. from three independent experiments. *P* value was determined by two-tailed unpaired *t*-test (B-E, G-J) or two-way ANOVA with Holm-Šídák post-hoc test (K and L). ns, not significant; $^*P < 0.05$, $^{**}P < 0.01$, $^{***}P < 0.001$, $^{****}P < 0.0001$. The diagram in (A) was created using BioRender. Ku, G. (2025) https://BioRender.com/wm1srtz.

flux through alternative metabolic pathways when serum-derived substrates become limiting, supporting sustained energy production. This condition-specific metabolic adaptability provides a mechanistic basis for the enhanced survival and proliferation of NMSCs under TME-mimicking conditions, where reduced ROS generation and stable mitochondrial function protect against oxidative damage while metabolic flexibility enables sustained energy production under resource constraints. The improved metabolic parameters observed in NMSCs suggested potential downstream effects on cell survival and proliferation pathways. To investigate this relationship further, we first examined the impact of NQO1 on apoptotic resistance under various stress conditions. Flow cytometric analysis using Annexin V/ PI staining revealed significantly reduced early apoptotic Annexin V^+ cell populations in NMSCs compared to control MSCs, with particularly clear differences observed under nutrient-deprived conditions (Fig. 2J). Under serum deprivation, NMSCs exhibited 21.53 % fewer apoptotic cells than control MSCs ($P = 0.0001$), while under combined hypoxia and serum deprivation, this protection was maintained with a 31.77 % reduction in apoptosis ($P < 0.0001$). These results demonstrate that NQO1 enhancement provides robust protection against apoptosis across various stress conditions that characterize the TME.

To determine whether this enhanced survival translated to functional benefits in cell growth and persistence, we conducted cell proliferation assays under all four stress conditions. Under normoxic conditions, NMSCs demonstrated accelerated proliferation compared to control MSCs, expanding 1.53-fold more than controls by day 4 (Fig. 2K, left). This growth advantage was similarly observed under hypoxic conditions (Fig. 2K, right). More strikingly, under severe nutrient deprivation and hypoxic stress conditions, where cell death rather than proliferation was the predominant response, NMSCs exhibited significantly enhanced survival capacity. While both cell types showed declining numbers under serum deprivation, NMSCs exhibited 55.66 % enhanced survival by day 2 ($P = 0.0073$) (Fig. 2L, left). Similarly, under combined stress, NMSCs showed significantly improved persistence, with 61.18 % greater cell retention after two days compared to control MSCs ($P = 0.0004$) (Fig. 2L, right). Collectively, these data demonstrate that NQO1-mediated metabolic improvements translate directly into enhanced cellular persistence under conditions that closely mimic the challenging tumor environment.

To further evaluate NMSC resilience in the TME, we examined their performance under acidic conditions (pH 6.5), another critical stress factor in solid tumors [46] (Fig. S2A). Consistent with the protective phenotype observed across other stress conditions, NMSCs maintained their protective advantages, demonstrating significantly reduced ROS levels, enhanced mitochondrial membrane potential, decreased apoptosis, and superior proliferation capacity with 2.77-fold higher cell numbers by day 4 ($P < 0.001$) compared to control MSCs (Fig. S2B-F). This reproducible pattern of enhanced redox homeostasis, mitochondrial stability, and apoptotic resistance across diverse stress environments validates the robustness of NQO1-mediated protection. Additionally, OCR analysis confirmed that NMSCs maintained their characteristic efficiency-oriented metabolic phenotype even under acidic stress, further supporting their resilience across TME-associated stresses (Fig. S2G-J).

These comprehensive analyses reveal that NQO1 enhancement provides MSCs with significantly improved resilience against multiple stress conditions prevalent in the TME. The protective effects span from fundamental metabolic improvements to enhanced cellular survival and proliferation, highlighting the potential of NQO1-enhanced MSCs as robust delivery vehicles capable of sustained therapeutic protein production within hostile TME.

2.4. Prolonged persistence and localized delivery of IP10-Fc by NIP-MSC in the TME

Having established the survival benefits of NQO1 overexpression *in vitro*, we next investigated whether these advantages translated to enhanced persistence within the challenging TME *in vivo*. Before evaluating MSCs persistence, we first confirmed that MSCs alone do not promote tumor growth, as this has been a concern in the field [47]. Comparative analysis across MC38, B16, and CT26 syngeneic models showed no significant differences in tumor growth between MSC-treated and untreated controls (Fig. S3), establishing that MSCs lack intrinsic tumor-promoting activity in our experimental conditions. We administered carboxyfluorescein succinimidyl ester (CFSE)-labeled MSCs or NMSCs into tumor-bearing mice and analyzed their retention after 72 h using flow cytometry (Fig. 3A). NMSCs demonstrated significantly improved tumor persistence, with 59.45 % higher retention compared to control MSCs (Fig. 3B). Importantly, biodistribution analysis revealed that both cell types remained predominantly localized within the tumor tissue, with minimal detection in lymph nodes, lungs, spleen, or peripheral blood (Fig. 3C), consistent with our previous observations of preferential tumor tropism of MSC [48,49]. These results confirm that NQO1 enhancement not only improves MSC survival *in vitro* but also translates to persistency within the TME.

Based on these promising results, we engineered both of MSCs and NMSCs to produce IP10-Fc (designated as IP-MSC and NIP-MSC, respectively). Flow cytometry analysis confirmed that genetic modification did not compromise the expression of key MSC surface markers, with all engineered cell types maintaining expression of CD105, Sca1, and CD44 (Fig. S4). We then evaluated their protein production capacity under various stress conditions. Across all tested conditions, NIP-MSCs produced significantly higher levels of IP10-Fc compared to IP-MSCs, further validating the functional relevance of NQO1-mediated stress resistance (Fig. 3D, Fig. S2K). To confirm that the IP10-Fc produced by these engineered cells retained its biological activity, we performed T cell migration assays using a transwell system (Fig. 3E, left). NIP-MSC-conditioned media significantly enhanced T cell migration compared to control serum free media and MSC-conditioned media, and was comparable to the effect observed with recombinant IP10-Fc, demonstrating the functionality of the secreted protein (Fig. 3E, right). We established the expression system using the strong EF1α promoter [50], which showed higher recruiting capacity than the weaker SV40 promoter (Fig. S5A). The presence of the fused human IgG Fc domain did not significantly affect chemotactic activity (Fig. S5B). These results confirm that NQO1-enhanced MSCs exhibit improved survival and enhanced therapeutic protein production without compromising bioactivity.

To test the biodistribution of IP10-Fc, MC38 bearing mice were treated with IP10-Fc (10 μg) or NIP-MSCs (1.5×10^6) and IP10-Fc levels

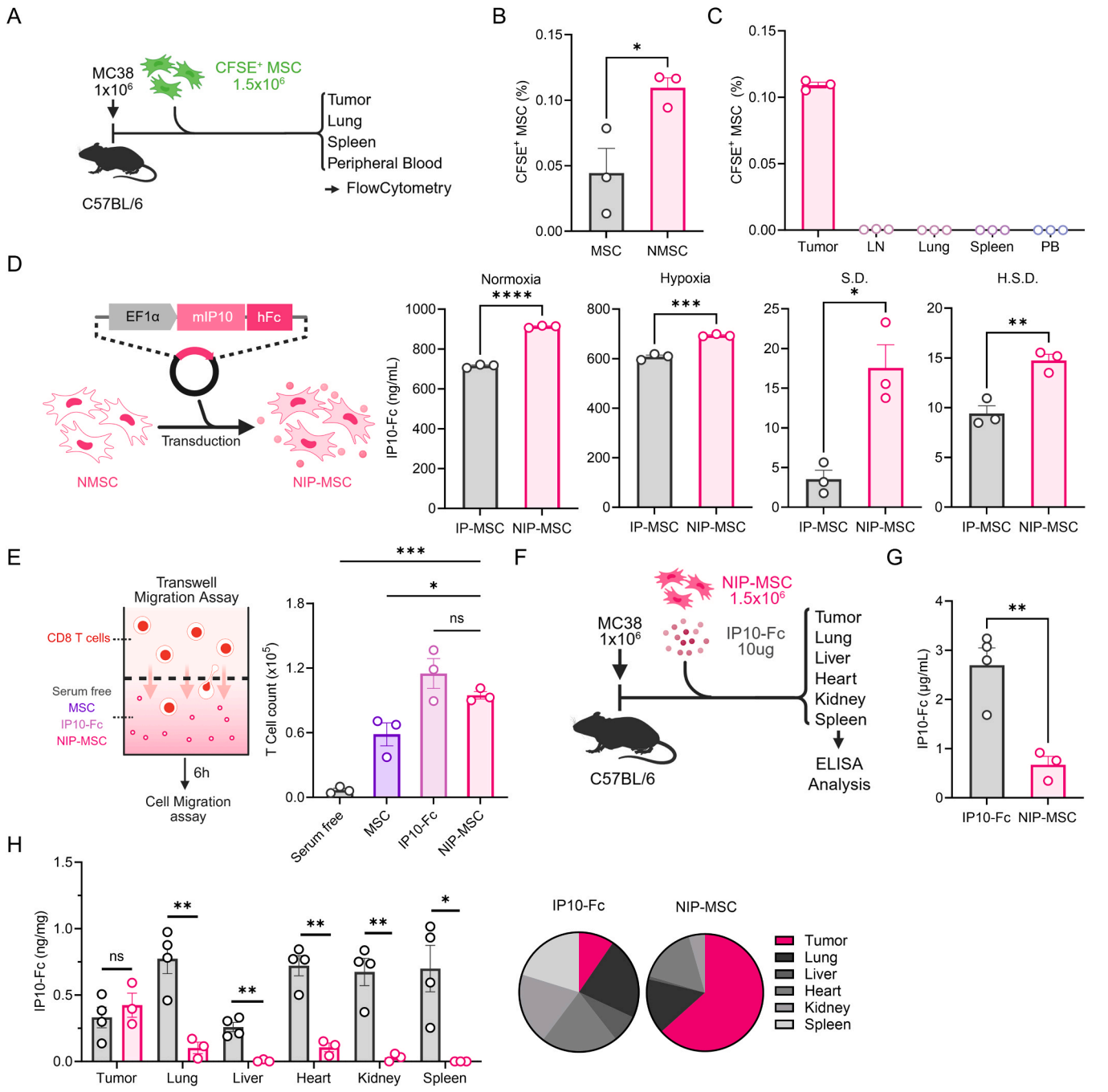


Fig. 3. NIP-MSCs achieve tumor-specific delivery of IP10-Fc with minimal systemic leakage. (A) Schematic of MSC biodistribution experiment. (B and C) C57BL/6 mice (n = 3) were s.c. inoculated with 1×10^6 MC38 cells. Ten days after tumor inoculation, 5×10^5 CFSE-labeled MSCs or NMSCs were p.t. injected. After 72 h, the percentage of $CFSE^+$ MSCs in tumor (B) and various tissues (C) were analyzed by flow cytometry. (D) IP10-Fc produced by IP-MSCs and NIP-MSCs were measured using ELISA. Cells were cultured under various stress conditions for 24 h (n = 3). (E) Transwell migration assay schematic (left) and quantification of migrated T cells toward IP10-Fc protein containing media, MSC or NIP-MSC conditioned media (right) (n = 3). (F) Schematic of IP10-Fc biodistribution following NIP-MSC delivery. (G and H) C57BL/6 mice (n = 5) were s.c. inoculated with 1×10^6 MC38 cells. Ten days after tumor inoculation, 20 μg IP10-Fc was i.t. injected or 5×10^5 NIP-MSCs were p.t. injected. After 6 h, serum concentration (G) and tissue biodistribution (H) of IP10-Fc were determined by ELISA. Data are shown as mean ± s.e.m. from two independent experiments. *P* value was determined by two-tailed unpaired *t*-test (B, D and G) or one-way ANOVA with Holm-Šídák post-hoc test (E and H). $^*P < 0.05$, $^{**}P < 0.01$, $^{***}P < 0.001$, $^{****}P < 0.0001$. The diagram in (A), (D), (E) and (F) were created using BioRender. Ku, G. (2025) https://BioRender.com/euhyf1u.

in tissue were investigated (Fig. 3F). Remarkably, NIP-MSC injection resulted in significantly lower systemic leakage of IP10-Fc in serum (0.67 ± 0.17 μg/mL) compared to direct injection of IP10-Fc (2.70 ± 0.35 μg/mL) (Fig. 3G). Importantly, organ distribution analysis demonstrated that NIP-MSC treatment achieved equivalent intratumoral IP10-Fc concentrations compared to direct protein injection, while dramatically improving tumor selectivity (Fig. 3H, left). The pie charts clearly show that while recombinant IP10-Fc distributed broadly across multiple organs, NIP-MSC-derived IP10-Fc demonstrated predominant tumor localization with minimal systemic distribution (Fig. 3H, right). This clear difference in biodistribution patterns highlights the superior targeting capability of cell-based delivery systems, creating a focused chemokine gradient within the tumor while virtually eliminating off-target accumulation compared to direct protein administration.

Taken together, these observations indicate that engineered MSCs expressing NQO1 and IP10-Fc not only survive better within the TME but also provide a superior platform for localized, sustained delivery of IP10-Fc, which may lead to the formation of an effective concentration gradient, supporting optimal immune cell recruitment and potentially overcoming the biodistribution challenges observed with direct IP10-Fc administration.

2.5. NIP-MSCs demonstrate enhanced anti-tumor efficacy through increased T cell infiltration into the tumor site

To evaluate the therapeutic efficacy of NIP-MSCs *in vivo*, MC38 bearing mice were peritumorally administered either MSCs or NIP-MSCs when tumors reached approximately 100 mm^3 (Fig. 4A). NIP-MSC treatment group showed prolonged survival ($P = 0.0195$) (Fig. 4B) with one complete regression and significantly reduced tumor burden ($P = 0.0014$) (Fig. 4C, Fig. S6A). To confirm the broad applicability of this efficacy, we tested NIP-MSCs in two additional models with distinct immunological profiles: the poorly immunogenic B16 melanoma and the highly immunogenic CT26 colon carcinoma. In both models, NIP-MSC treatment resulted in significant tumor growth inhibition, demonstrating a robust and reproducible anti-tumor activity (Fig. S6B, C). To elucidate the mechanisms underlying this enhanced anti-tumor effect, we performed comprehensive flow cytometric analysis of tumor-infiltrating lymphocytes (TILs) (Fig S7A). NIP-MSC treatment resulted in substantially increased infiltration of $CD3^+$ T cells compared to control MSC treatment ($P = 0.0705$) (Fig. 4D). Further characterization revealed a significant increase in $CD8^+$ cytotoxic T lymphocytes within the TME of NIP-MSC-treated mice (Fig. 4E). Interestingly, analysis of T cell activation status showed a marked increase in $PD1^+$ $CD8^+$ T cells, which represent antigen-experienced T cells with enhanced effector potential [51,52] (Fig. 4F). Notably, this included a substantial population of $PD1^+$ $TIM3^+$ double-positive cells, which, despite their exhausted phenotype, retain potent cytotoxic capacity against tumor cells [53–55] (Fig. 4G).

Given that the observed anti-tumor effects could potentially result from the recruitment of other CXCR3-expressing immune cell populations beyond $CD8^+$ T cells, we conducted comprehensive immunophenotyping to characterize which immune subsets are attracted by NIP-MSC treatment and determine their respective contributions to therapeutic efficacy. As previously reported, lymphoid cells including NK cells, $CD8^+$ T cells, $CD4^+$ T cells, and regulatory T cells express CXCR3 [56], which was confirmed by flow cytometric analysis showing this broad CXCR3 expression pattern across multiple immune populations within the TME. Importantly, NIP-MSC treatment significantly enhanced the recruitment of these immune cell populations to the TME compared to control MSCs (Fig. 4I). To determine which immune subset conducts crucial role for antitumor effect of NIP-MSC, we performed systematic immune depletion experiments using neutralizing antibodies targeting specific cell subsets in mice bearing established MC38 tumors treated with NIP-MSCs. The neutralizing antibody-mediated immune subset depletion was verified by comparing immune cell proportion within the peripheral blood (Fig. S8). The results revealed striking differences in the functional importance of each population (Fig. 4J). NK cell depletion (αNK1.1) had no significant impact on NIP-MSC therapeutic efficacy. In stark contrast, $CD8^+$ T cell depletion (αCD8) completely abrogated the therapeutic benefit, with tumor growth actually accelerated compared to MSC controls, demonstrating that recruited $CD8^+$ T cells are essential for therapeutic efficacy. Most remarkably, $CD4^+$ T cell depletion (αCD4) resulted in enhanced tumor control compared to NIP-MSC treatment alone, likely due to elimination of immunosuppressive Tregs within the $CD4^+$ compartment, thereby unleashing a more potent $CD8^+$ T cell response.

Given previous reports that CXCL10 can directly influence T cell activation states [57,58], the observed T cell phenotype changes might be resulted from direct IP10-Fc effects on T cell. To address this possibility, we conducted *in vitro* experiments using mouse splenocytes cultured under T cell activation conditions (anti-CD3, anti-CD28, and IL-2) with or without IP10-Fc (Fig. 4K). IP10-Fc treatment had no direct effect on T cell exhaustion markers (Fig. 4L), activation markers (Fig. 4M), or cytokine production capacity (Fig. 4N). These results indicate that the enhanced T cell activation observed *in vivo* likely results from IP10-Fc mediated T cell recruitment into the TME, where prolonged T cell retention and subsequent engagement promote cytotoxic activity against tumor cells rather than direct immunomodulatory effects.

Collectively, these findings demonstrate that the enhanced anti-tumor efficacy of NIP-MSCs is primarily mediated by increased recruitment of T cells to the TME. The observed increase in exhausted T cells likely represents a consequence of prolonged T cell residence and sustained engagement within the immunosuppressive TME, facilitated by CXCL10-mediated chemotaxis. This mechanistic insight provides a rationale for combining CXCL10-based therapies with ICB, as enhanced T cell recruitment could synergize with strategies that reinvigorate exhausted T cells within the tumor, consistent with clinical evidence linking *CXCL10* expression to improved ICB responses [59,60].

2.6. NIP-MSCs selectively enhance recruitment of both endogenous and adoptively transferred T cells to the TME

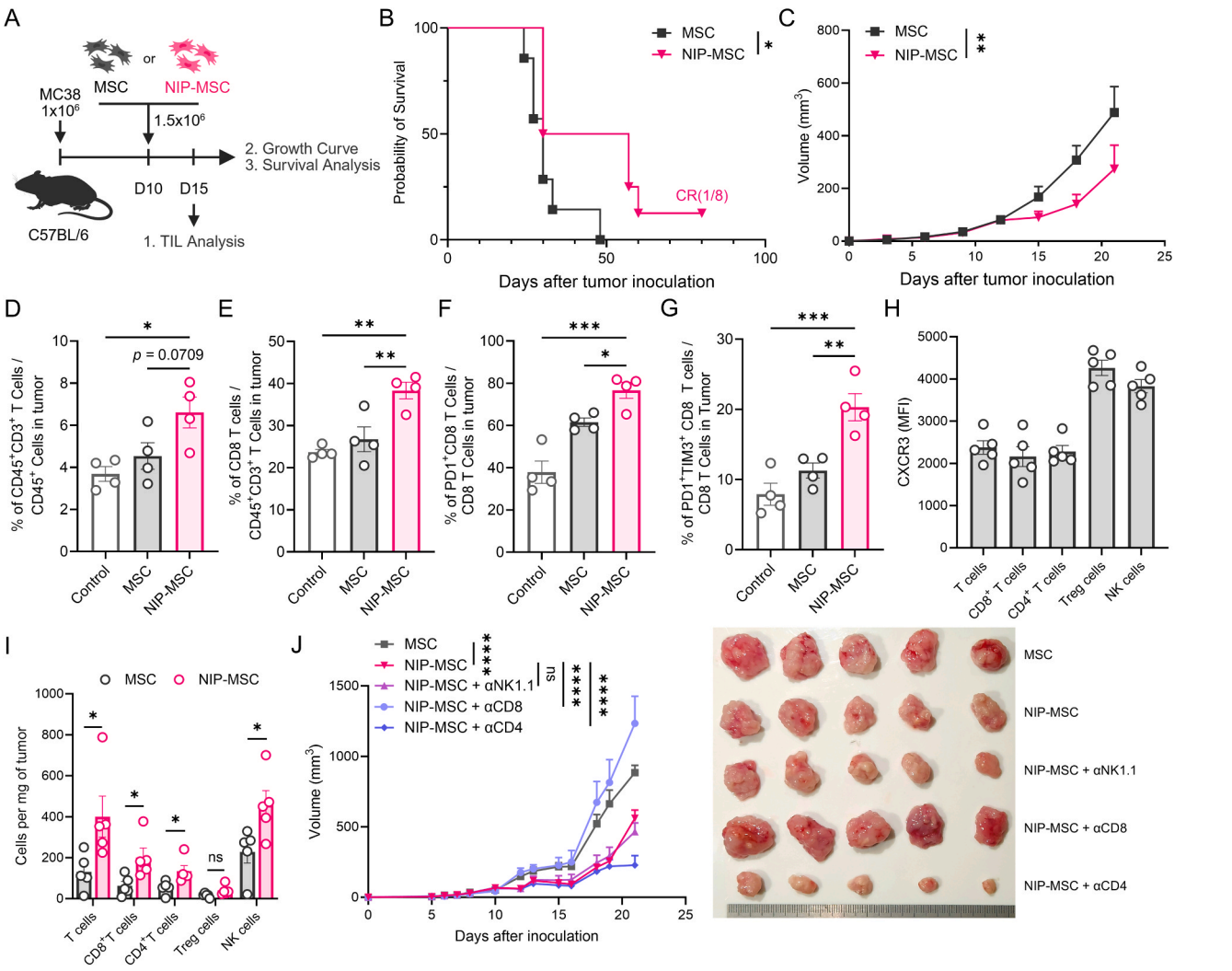
Given the T cell recruitment capacity of IP10-Fc, we hypothesized that NIP-MSCs could serve as an effective combinatorial approach for adoptive cell transfer (ACT) therapy by selectively enhancing T cell recruitment to tumors. We designed an experiment comparing the recruitment capacity for both endogenous and adoptively transferred T cells (Fig. 5A). We established B16-OVA tumors, an immunologically "cold" tumor model with typically poor T cell infiltration, in C57BL/6 mice and administered MSCs, IP10-Fc protein, or NIP-MSCs. T cells were labeled with CFSE before transfer to distinguish endogenous and transferred T cells. Endogenous ($CFSE^-$) and transferred ($CSFE^+$) T cell populations in the tumor, lungs, and tumor-draining lymph nodes (TdLN) were analyzed by flow cytometry (Fig. 5B and Fig. S7B).

Analysis of endogenous T cells revealed that NIP-MSC treatment significantly enhanced tumor infiltration compared to direct IP10-Fc administration (Fig. 5C, left), while no significant differences were observed in lung or TdLN T cell numbers (Fig. 5C, middle and right). This tumor-specific enhancement was likely due to the tumor-homing properties of MSCs. Importantly, the tumor-to-lung ratio of endogenous T cells, a critical parameter for assessing treatment specificity and potential off-target effects, was significantly higher in the NIP-MSC group compared to direct IP10-Fc injection (Fig. 5D), consistent with our earlier findings regarding improved concentration gradient establishment. (Fig. 4H) Most notably, when examining adoptively transferred T cells, we observed dramatically enhanced recruitment to the tumor in the NIP-MSC group compared to both control MSCs and direct IP10-Fc injection (Fig. 5E, left). No significant differences were detected in lung or TdLN infiltration (Fig. 5E, middle and right), resulting in huge tumor-to-lung ratio of transferred T cells in the NIP-MSC group (Fig. 5F), demonstrating the superior tumor-specific recruitment capability of NIP-MSCs for ACT.

Overall, NIP-MSCs selectively enhances the recruitment of both endogenous and adoptively transferred T cells specifically to the TME, suggesting their potential utility as a complementary strategy for ACT-based immunotherapies.

2.7. CXCL10 delivery within the TME potentiates the therapeutic effect of adoptively transferred T cells

Based on our findings that NIP-MSCs selectively enhance T cell recruitment to tumors, we next investigated whether this property could translate to improved therapeutic outcomes when combined with ACT therapy. B16-OVA bearing mice and administered either MSCs or NIP-



(caption on next page)

Fig. 4. Tumor-specific delivery of IP10-Fc suppress tumor growth through enhanced T cell infiltration. (A) Experimental design for NIP-MSC treatment in MC38 tumor model. (B–C) C57BL/6 mice (n = 7–8) were s.c. inoculated with 1×10^6 MC38 cells followed by 5×10^5 MSCs or NIP-MSCs p.t. administration on days 9 and 12. Tumor growth was measured twice weekly. (D to G) Five days after the last treatment, TILs were analyzed for percentage of $CD3^+$ T cells (D), CD8 T cells (E), $PD\text{-}1^+$ CD8 T cells (F), and $PD\text{-}1^+TIM\text{-}3^+$ CD8 T cells (G) (n = 5–6 per group). (H-J) Mice were subcutaneously inoculated with 1.0×10^6 MC38 cells. When tumor volumes reached 50 mm^3, mice were treated with 1.5×10^6 NIP-MSCs or control MSCs. Mean Fluorescence Index (MFI) of CXCR3 in infiltrated lymphocytes (H) and absolute counts of each immune cell subset in tumor normalized by tissue weight (I) in MC38 at the end point. (J) Anti-CD8 (200 μg), anti-CD4 (200 μg) and anti-NK1.1 (200 μg) were administered via i.p. injection twice a week for two weeks, starting the day before MSC injection. Data show tumor growth curves (left) and representative photographs of the tumor (right). (K) Schematic of in vitro T cell activation experiment. (L to N) Mouse splenocytes were activated with anti-CD3/CD28 and IL-2, in the presence or absence of 1 μg/mL IP10-Fc for 72 h (n = 3). PD-1 and TIM-3 expression profile (L), MFI of activation/exhaustion markers (M), and intracellular cytokine levels (N) were analyzed by flow cytometry. Data are shown as mean ± s.e.m. from two or three independent experiments. *P* value was determined by log-rank test (B), two-way ANOVA with Holm-Šídák post-hoc test (C and J), one-way ANOVA with Holm-Šídák post-hoc test (D-G, I) or two-tailed unpaired *t*-test (L-N). ns, not significant; $^*P < 0.05$, $^{**}P < 0.01$, $^{***}P < 0.001$. The diagram in (A) and (K) were created using BioRender. Ku, G. (2025) https://BioRender.com/uawbvrp.

MSCs, followed by adoptive transfer of OT-I $CD8^+$ T cells. To enhance the engraftment and expansion of transferred T cells, we performed lymphodepletion with cyclophosphamide (CTX) one day prior to cell therapy, following clinically established protocols [61,62] (Fig. 6A). Long-term survival analysis revealed that while neither MSC nor NIP-MSC monotherapy provided durable protection, and MSC treatment with ACT offered modest survival benefit, the combination of NIP-MSC with ACT significantly extended survival compared to all other groups (Fig. 6B). This improved survival correlated with superior tumor growth control, as evidenced by significantly reduced tumor volumes in the NIP-MSC and ACT combination treatment group (Fig. 6C, D). The combination of MSCs with ACT showed minimal improvement compared to ACT alone (Fig. S9). Notably, NIP-MSCs demonstrated superior enhancement of ACT efficacy over IP-MSCs, which is likely attributable to the benefits of the dual engineering platform, enabling prolonged IP10-Fc production through NQO1-mediated cellular persistence in the harsh TME. These results demonstrate that NIP-MSCs provide substantial therapeutic benefit when combined with ACT, translating enhanced T cell recruitment into meaningful survival advantages.

To understand the mechanism behind this enhanced therapeutic efficacy, we performed flow cytometric analysis of TILs. Consistent with our hypothesis, the NIP-MSC and ACT combination treatment group showed significantly higher numbers of tumor-infiltrating OT-I T cells compared to the NMSC and ACT combination treatment group (Fig. 6E). Importantly, this enhanced recruitment was tumor-specific manner, as no significant differences in OT-I T cell numbers were observed in the lungs, TdLN, or peripheral blood (Fig. 6F) between treatment groups. This selective tumor accumulation of transferred T cells without systemic toxicity represents an ideal therapeutic profile for combination immunotherapy.

Collectively, our results establish that NIP-MSCs can significantly augment the efficacy of adoptive T cell therapy by selectively enhancing the recruitment and accumulation of tumor-specific T cells within the TME, without affecting their systemic distribution. Tumor-specific T cell infiltration translates to improved tumor control and prolonged survival, highlighting the potential of NIP-MSCs as an effective complementary strategy for ACT-based immunotherapies.

3. Discussion

The limited infiltration of T cells into solid tumors remains one of the major challenges to successful cancer immunotherapy [3,63,64]. While chemokines like CXCL10 have well-established roles in T cell recruitment, their therapeutic application has been hampered by poor pharmacokinetics, systemic leakage, and inability to maintain effective concentration gradients within tumors [15,65]. Our study addresses these fundamental challenges through a novel engineered cellular platform that combines enhanced MSCs persistence and localized IP10-Fc delivery within the TME, demonstrating significant therapeutic benefits in multiple murine cancer models.

The concept of using engineered cells to deliver CXCL10 for cancer immunotherapy has gained increasing recognition in recent years [22,66,67]. Concurrent with our work, other researchers have explored similar approaches across different cancer types and delivery platforms. Notably, engineered dendritic cells expressing CXCL9 and CXCL10 have shown promise in overcoming ICB resistance in non-small cell lung cancer, demonstrating enhanced T cell infiltration and tumor control when combined with PD-1/PD-L1 inhibition [66]. Similarly, a recent study in glioblastoma employed Nrf2-enhanced MSCs delivering CXCL10 to overcome the blood-brain barrier and improve T cell infiltration in brain tumors, with particularly promising results when combined with ICB [67]. These findings demonstrate the therapeutic potential of sustained intratumoral CXCL10 delivery and validate our cell-based approach for overcoming systemic protein leakage challenges.

Our work extends beyond these previous studies by providing several key innovations and insights. First, MSCs as the delivery vehicle provides a strong foundation for clinical translation, given their well-established clinical safety profile from numerous clinical trials [68]. Second, this approach proactively addresses the fundamental challenge of limited cell persistence within the hostile TME. The dual-engineering strategy combining NQO1 enhancement with CXCL10 delivery enables prolonged chemokine production in harsh TME. The comprehensive characterization of protective effects of NQO1, from NAD^+/NADH ratio maintenance to mitochondrial protection and overall cellular resilience, establishes a mechanistic foundation for this enhancement strategy that could be broadly applicable to other cell-based therapies. Third, rigorous biodistribution analysis confirms that these features culminate in a highly localized and stable chemokine gradient, ensuring effective T cell recruitment while minimizing systemic exposure—a critical aspect for both safety and efficacy [28,69,70]. Finally, our detailed analysis of both endogenous and adoptively transferred T cell trafficking patterns provides crucial insights for combination immunotherapy applications, particularly demonstrating how cellular delivery of CXCL10 can create high concentration gradient and tumor-specific chemotaxis without systemic leakage.

The observation that IP10-Fc enhanced T cell recruitment without directly modulating T cell functional states provides important mechanistic clarity. We observed increased numbers of both $PD\text{-}1^+$ activated and $PD1^+TIM3^+$ exhausted T cells within tumors, consistent with enhanced tumor engagement rather than direct immunomodulatory effects. These findings not only highlight the role of CXCL10 in enhancing T cell recruitment but also support the potential benefit of combining CXCL10-based strategies with ICB therapy [66,67]. The therapeutic synergy observed between NIP-MSCs and adoptive cell transfer is particularly promising for clinical translation. Current ACT approaches, including tumor-infiltrating lymphocyte therapy and engineered T cell therapies like chimeric antigen receptor (CAR)-T cells, often face challenges with insufficient tumor infiltration despite robust peripheral expansion. NIP-MSCs can significantly enhance the tumor-specific accumulation of transferred T cells without affecting systemic distribution suggests this approach could reduce the therapeutic dose of CAR-T cell while preventing on-target off-tumor effects

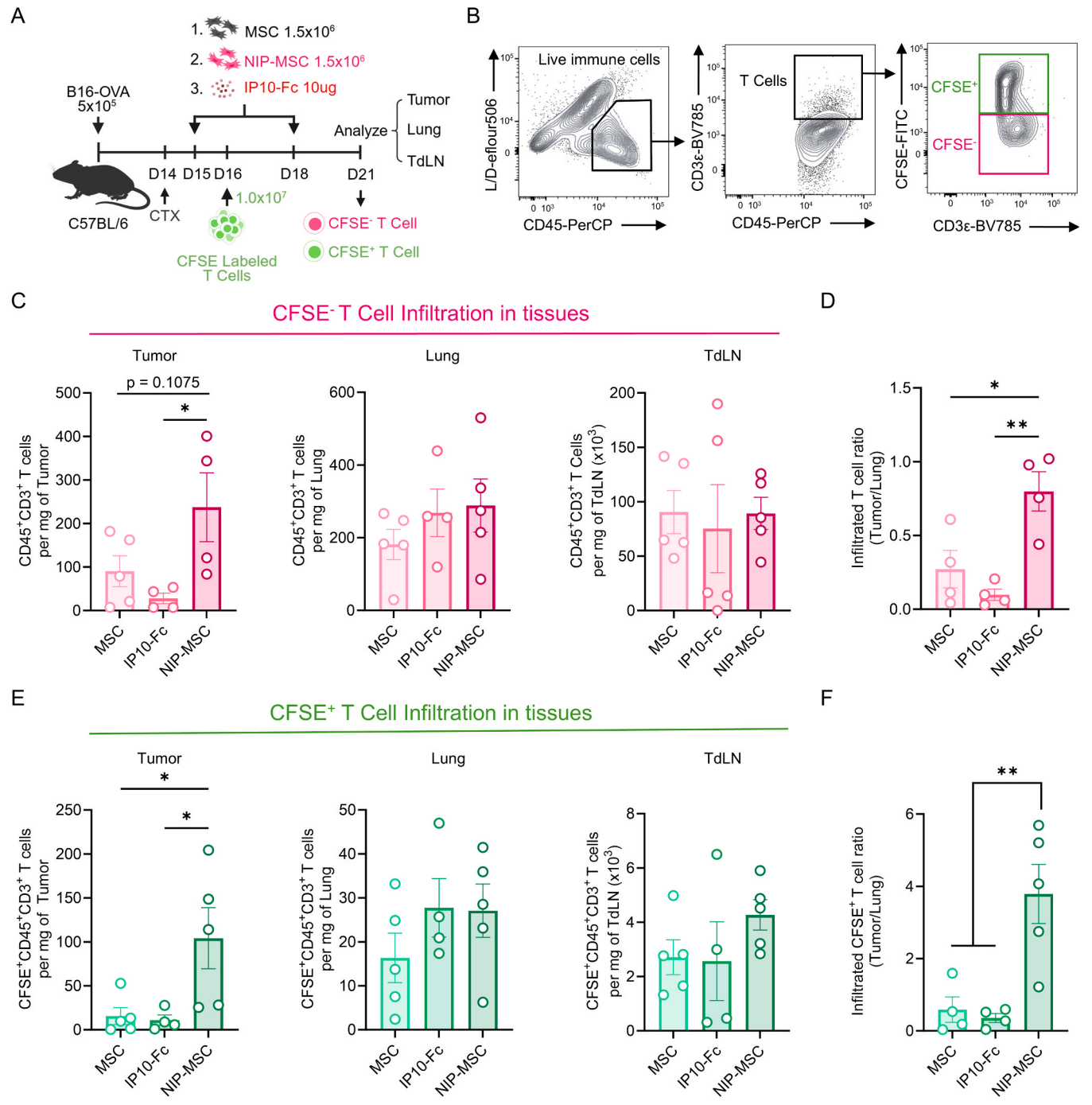


Fig. 5. NIP-MSCs recruit endogenous and adoptively transferred T cells to tumors. (A) Experimental design for T cell biodistribution assay. (B) Representative contour plots showing gating strategy to distinguish endogenous ($CFSE^-$) and adoptively transferred ($CFSE^+$) T cells. (C-F) C57BL/6 mice (n = 5) were s.c. inoculated with 1×10^6 B16-OVA cells. Nine days after tumor inoculation, MSCs (5×10^5, p.t.), IP10-Fc (20 μg, i.t.), or NIP-MSCs (5×10^5, p.t.) were administered followed by CFSE-labeled T cells (1×10^6, i.v.) administration on day 10. (C) Three days later, absolute counts of $CFSE^-$ endogenous T cells in tumor, lung, and TdLN were normalized by tissue weight. (D) Tumor-to-lung ratio of endogenous T cells were calculated from normalized counts. (E) Three days later, absolute counts of $CFSE^+$ exogenous T cells in tumor, lung, and TdLN were normalized by tissue weight. (F) Tumor-to-lung ratio of adoptively transferred T cells were calculated from normalized counts. Data are shown as mean ± s.e.m. from two or three independent experiments. *P* value was determined by one-way ANOVA with Holm-Šídák post-hoc test (C-F). $*P < 0.05$, $**P < 0.01$. The diagram in (A) was created using BioRender. Ku, G. (2025) https://BioRender.com/2go5g20.

and systemic toxicities such as cytokine release syndrome.

A key technical advantage of our approach lies in the superior biodistribution profile achieved through cellular delivery. The distinct contrast between systemic IP10-Fc levels from protein injection versus NIP-MSC mediated delivery demonstrates how cellular platforms can overcome key limitations of chemokine-based therapies, particularly the challenge of establishing and maintaining precise chemotactic gradients at target sites while minimizing off-target effects [28,70,71]. However, several aspects warrant further optimization to maximize clinical utility. First, the duration of NIP-MSC persistence and IP10-Fc production requires detailed characterization to inform optimal dosing schedules and treatment intervals. Second, implementing TME-responsive inducible expression systems could enhance therapeutic precision by tailoring protein production to local conditions. Finally, incorporating safety

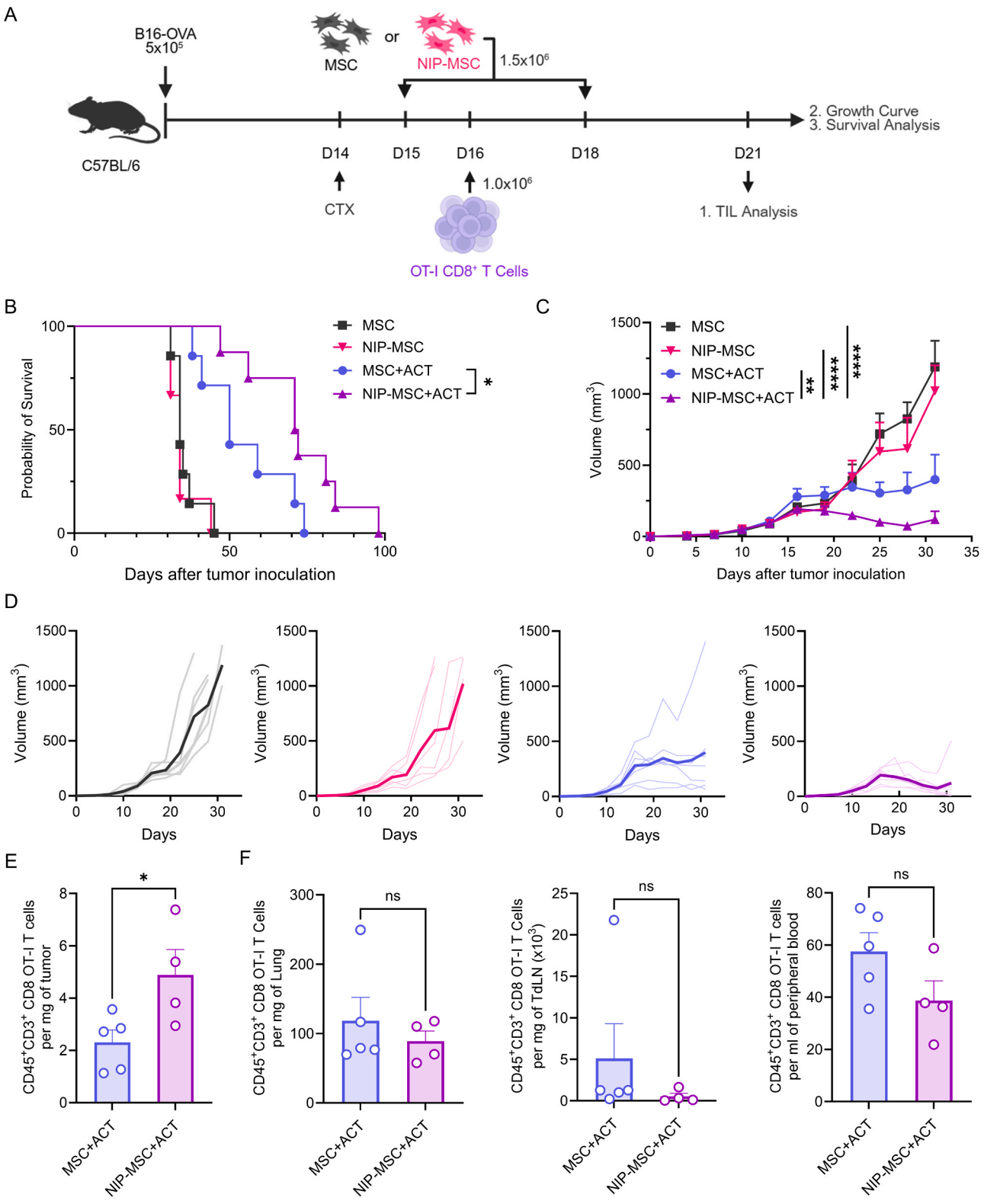


Fig. 6. NIP-MSCs enhance therapeutic efficacy of adoptive T cell transfer. (A) Experimental design for combination therapy with NIP-MSCs and ACT. (B-D) C57BL/6 mice (n = 8–10) were s.c. inoculated with 5×10^5 B16-OVA cells. Eight days after tumor inoculation, mice received cyclophosphamide (100 mg/kg, i.p.). On day 9, MSCs or NIP-MSCs (5×10^5, p.t.) were injected followed by OT-I T cells (5×10^6, i.v.) administration. Survival (B) and tumor growth (C-D) were monitored. (E and F) Seven days after ACT, absolute counts of OT-I T cells in tumor (E) and other tissues (F) were normalized by tissue weight or blood volume (n = 5–6 per group). Data are shown as mean ± s.e.m. from two or three independent experiments. *P* value was determined by log-rank test, two-way ANOVA with Holm-Šídák post-hoc test (C), or two-tailed unpaired *t*-test (E and F). ns, not significant; $^*P < 0.05$, $^{**}P < 0.01$, $^{***}P < 0.001$, $^{****}P < 0.0001$. The diagram in (A) was created using BioRender. Ku, G. (2025) https://BioRender.com/m97qk9v.

switch mechanisms, such as those demonstrated in IL-2 therapies [49], could provide enhanced control and reversibility for improved clinical safety profiles.

The broader implications of our findings extend well beyond CXCL10 delivery to the field of cellular therapeutics. The NQO1-enhancement strategy could improve the persistence and efficacy of various cell-based therapies operating in challenging microenvironments, while our approach to creating localized protein gradients through cellular production could be extended to other therapeutic proteins requiring precise spatial distribution, such as promoting tertiary lymphoid structures (TLS), which are associated with improved immunotherapy responses [72,73]. From a translational perspective, our platform offers compelling advantages: MSCs have well-established clinical safety profiles [27], the genetic modifications involve well-characterized proteins, and their inherent tumor-tropic properties eliminate complex targeting requirements [28]. The demonstrated synergy with adoptive cell transfer, particularly the potential applications in CAR-T cell therapy, positions this approach for immediate clinical investigation as a complementary strategy to enhance existing cellular immunotherapies.

In conclusion, our engineered NIP-MSC platform addresses fundamental limitations in cancer immunotherapy by providing sustained, localized CXCL10 delivery that enhances T cell infiltration into the TME. The therapeutic benefits observed in both monotherapy and combination settings with ACT, highlight the potential of this approach to improve outcomes across diverse immunotherapy applications. As the field moves toward increasingly sophisticated combination strategies, tumor-targeted delivery of therapeutics using engineered MSCs may safely and effectively modify the TME, thereby overcoming the challenges of conventional therapies and potentiating their efficacy in solid tumors.

4. Materials and methods

4.1. Animals

Six-to-eight weeks old C57BL/6 N and C57BL/6J-Tg (TcraTcrb) 1100Mjb/J (OT-1 TCR transgenic) mice were purchased from The Jackson Laboratory (Bar Harbor, ME, USA) and bred in a specific pathogen-free environment under standard conditions with a 12 h light/dark cycle and ad libitum access to water and food. Inbred mice were employed for experiments after reaching 8 weeks of age. All experimental procedures, including animal breeding, were approved by the Animal Care Committee of Korea University in accordance with the guidelines and regulations of the Republic of Korea (KUIACUC-2024–0053, KUIACUC-2024–0085).

4.2. Cell lines and culture conditions

MC38, B16F10, and HEK293FT cell lines were purchased from American Type Culture Collection. MC38, B16F10, B16-OVA, HEK293FT, CT26 mouse bone marrow-derived mesenchymal stem cells (BM-MSCs), and engineered MSCs were cultured in Dulbecco's Modified Eagle's Medium (Welgene, Gyeongsangbuk-do, Korea; LM001–01) supplemented with 10 % fetal bovine serum (FBS) (Welgene; S001–01) and 100 U/mL penicillin-streptomycin (Welgene; LS202–02). The mouse BM-MSCs were obtained from the bone marrow of female C57BL/6NCrlOri mice and immortalized as previously described [49]. CHO-S cells were maintained in ExpiCHO Expression Medium (Thermo Fisher Scientific, Waltham, MA, USA; A29010001).

Mouse T cells were isolated from spleen and lymph nodes and cultured in RPMI 1640 medium (Welgene; LM011–01) supplemented with 10 % FBS, 100 U/mL penicillin-streptomycin, 1 mM sodium pyruvate (Thermo Fisher Scientific; 11360070), 20 mM HEPES (Welgene; BB001–01), MEM non-essential amino acids solution (Thermo Fisher Scientific; 11140050), and β-mercaptoethanol (Thermo Fisher Scientific; 21985023). For *in vitro* activation, isolated T cells were stimulated with plate-coated anti-mouse CD28 (2 μg/mL; BD Biosciences; 102102) in the presence of recombinant human IL-2 (5 ng/mL; Thermo Fisher Scientific; 200–02–50UG). After 48 h of *in vitro* activation, T cells were considered activated and harvested using ice-cold Dulbecco's phosphate-buffered saline (DPBS) (Welgene; LB001–02).

All cells were maintained at 37 ℃ in a humidified atmosphere containing 5 % CO_2. Hypoxic conditions were achieved by incubating cells in a Modular Incubator Chamber (Embrient Inc., San Diego, CA, USA; MIC-101) filled with hypoxia gas composed of 5 % CO_2 and 1 % O_2, balanced with N_2. Serum-free media were used when indicated to achieve serum-deprivation conditions. Adherent cells were passaged before reaching 80 % confluency using 1 × Trypsin-EDTA solution (Welgene; LS015–01). All cell lines were confirmed to be mycoplasma-free.

4.3. Generation of engineered MSCs

The lentiviral vector encoding the fusion protein of mouse Cxcl10 and human IgG Fc region (IP10-Fc) was generated from the coding sequences of mouse Cxcl10 (NM_0212274) and human IgG Fc region (MW_176591). LALAPG mutations were introduced to eliminate complement activity and reduce binding affinity to Fcγ receptors. A separate lentivirus vector for NQO1 overexpression was constructed using mouse Nqo1 (NM_008706) sequence.

For lentivirus production, HEK293FT cells were transfected with expression vectors and packaging vectors pMDLg/pRRE, pRSV-Rev, and the envelope pMD2.G (#12251, #12252, #12259, respectively, all procured from Addgene) using Lipofectamine 3000 (Thermo Fisher Scientific; L3000–008) according to the manufacturer's protocol. The culture medium containing the lentivirus was harvested at 48 and 72 h post-transfection and concentrated using a Lenti-X concentrator (Takara, Nojihigashi, Kusatsu, Japan; 631231). The concentrated lentiviral particles were transduced into immortalized MSCs using hexadimethrine bromide (polybrene) at 8 μg/mL (Sigma-Aldrich, Burlington, MA, USA; TR-1003), with centrifugation (1000 g for 1 h at room temperature) to enhance transduction efficiency. Successfully transduced MSCs were selected with either 5 μg/mL puromycin (Thermo Fisher Scientific; A1113803) or 600 μg/mL G418 (InvivoGen, San Diego, CA, USA; ant-gn-1).

4.4. Protein purification and quantification

For protein purification, IP10-Fc expression vector was transfected into 293-F cells as previously described [74]. Following standard transfection and feeding protocols, conditioned media were harvested after 3 days and subjected to protein A affinity chromatography. Bound proteins were eluted with glycine buffer (pH 3.0) and protein concentration was determined using standard Bradford assay methods. The purity of protein was examined by SDS-PAGE.

4.5. Enzyme-linked immunosorbent assay (ELISA)

Fc-specific ELISA was performed using 96-well immunoplates (SPL Life Sciences, Gyeonggi-do, Korea; 32296) coated overnight at 4 ℃ with Fc-specific anti-human IgG capture antibody (2 μg/mL; Sigma-Aldrich; I2136) diluted in 0.1 M $NaHCO_3$. After washing with 0.05 % Tween20 (Sigma-Sldrich; P1379) in DPBS and blocking with 1 % bovine serum albumin (BSA, GenDepot, Katy, TX, USA; A0100) solution in DPBS, samples were added and incubated at room temperature in the dark for 1.5 h. Follwing an additional 3-times washing step, anti-human IgG (Fc specific)-peroxidase antibody (Sigma-Aldrich; A0170) diluted in 1 % BSA solution was added and incubated at room temperature in the dark for 1 h. Finally plates were developed by adding 100 μL 3,3′,5,5′-Tetramethylbenzidine (TMB) substrate solution (Thermo Fisher Scientific; N301), and the reaction was stopped with 100 μL of 3 M HCl (Sigma-Aldrich; 258148). Protein concentrations were determined by regression of OD_{450} values using a 5-parameter logistic standard curve, measured

with a HIDEX Sense 425–301 microplate reader (HIDEX Oy, Turku, Finland).

4.6. Immunoblot analysis

MSCs lysates were prepared as previously described [75] and subjected to SDS-PAGE using Bis-Tris polyacrylamide gels prepared in-house. Proteins were transferred onto polyvinylidene difluoride membranes (Merck Millipore, Darmstadt, Germany: IPVH00010). After blokcing with 5 % skimmed milk, membranes were immunoblotted with priamry antibodies aginst NQO1 (Cell Signaling Technology, Danvers, MA, USA; 62262) or β-actin (Santa Cruz Biotechnology, Inc., Dallas, TX, USA; sc-47778), followed by horseradish peroxidase-conjugated mouse anti-rabbit IgG secondary antibodies (Santa Cruz Biotechnology, Inc.; sc-2357) or horse anti-mouse IgG secondary antibodies (Cell Signaling Technology; 7076 s). Immunoreactive bands were visualized using Pierce™ ECL Western Blotting Substrate (Thermo Fisher Scientific; 32106) and analyzed using ImageJ.

4.7. Cellular NAD^+/NADH measurement

The NAD^+/NADH ratio was assessed using the NAD^+/NADH Assay kit (Abcam, Cambridge, UK; ab65348) according to the manufacturer's instructions. Briefly, cells were harvested and lysed with the provided extraction buffer, followed by heating at 60 ℃ for 30 min. After the heating step, samples were incubated for 2 h during reaction cycles and analyzed using a HIDEX Sense 425–301 microplate reader at designated time points before reaction termination.

4.8. Flow cytometry

Cells were harvested and resuspended in DPBS supplemented with 2 % FBS. When necessary, Fcγ receptors were blocked using anti-FcγIII/II receptor (clone 2.4G2) for 15 min to prevent non-specific binding. Fixable viability dye eFluor506 (Thermo Fisher Scientific; 65–0866–14) was used to identify live cells. Surface marker staining was performed using fluorescence-conjugated antibodies for 30 min at 4°C in the dark, with detailed antibody information provided in Supplementary Table 1. Intracellular marker staining was performed using fluorescence-conjugated antibodies for 50 min at 4°C in the dark (detailed in Supplementary Table 1). Before staining, cells were fixed using the True-Nuclear Transcription Factor Buffer Set (BioLegend; 424401) according to the manufacturer's protocol. Briefly, fixation step and permeabilization step were performed after cell surface staining using fluorescence-conjugated antibodies. Data were acquired on a NovoCyte Advanteon flow cytometer (Agilent, Santa Clara, CA, USA) and analyzed using NovoExpress (Agilent Technologies) or FlowJo (BD Biosciences) software.

4.9. Mitochondrial function analysis

Mitochondrial function was assessed by measuring reactive oxygen species (ROS) levels and membrane potential. For ROS detection, cells were harvested and stained with either H2DCFDA (Thermo Fisher Scientific; D399) for total ROS assessment or mitoSOX Mitochondrial Superoxide Indicators (Thermo Fisher Scientific; M36008) for mitochondrial ROS measurement. Final concentrations were 10 μM for H2DCFDA and 5 μM for mitoSOX. For mitochondrial membrane potential analysis, cells were stained with JC-1 (MedChemExpress, Monmouth Junction, NJ, USA; HY-15534) at a final concentration of 2 μM. Following 30 min incubation at 37°C, stained cells were washed with DPBS and resuspended for flow cytometric analysis. ROS levels were determined by mean fluorescent intensity, and mitochondrial membrane potential was calculated as the ratio between JC-1 aggregate and monomer.

4.10. Measurement of Oxygen Consumption Rate (OCR)

MSCs and NMSCs were seeded into a Seahorse XF Pro M cell culture microplate at a density of 2.0×10^4 cells/well. The cells were then cultured for 24 h under various stress conditions; normoxia, hypoxia, serum deprivation (S.D.), combined hypoxia and serum deprivation (H.S.D.) or acidosis. To chemically induce hypoxia, the culture medium was supplemented with 50 μM of $CoCl_2$. Prior to the assay, the culture medium was replaced with Seahorse XF Base Medium supplemented with 25 mM D-glucose, 4 mM L-glutamine and 1 mM sodium pyruvate. The plate was subsequently incubated for 1 h at 37 °C in a non-CO_2 incubator for temperature and pH equilibration. A mitochondrial stress test was performed through the sequential injection of 1 μM oligomycin, 1 μM carbonyl cyanide-p-trifluoromethoxyphenylhydrazone (FCCP) and 1 μM rotenone/antimycin A mixture. OCR values were normalized to the total protein content of each well. Key parameters, including basal respiration, ATP-linked respiration and maximal respiration, were calculated from the normalized data. The samples were analyzed using a Seahorse XF Pro Analyzer (NFEC-2025–07–306941) at Ewha Fluorescence Core Imaging Center.

4.11. Cell viability and apoptosis analysis

Apoptotic profiles were detected using the BD Pharmingen™ FITC Annexin V Apoptosis Detection Kit I (BD Biosciences; 556547) and propidium iodide (Sigma-Aldrich; 537059) according to manufacturer's instructions. Briefly, harvested cells were washed twice with ice-cold DPBS and resuspended in 1 × binding buffer prepared by diluting 10 × binding buffer (BD Biosciences; 556454) in distilled water. For every 1.0×10^5 cells, 100 μL of binding buffer was used with the addition of 1 μL FITC Annexin V and 5 μL propidium iodide. After 15 min incubation at room temperature in the dark, 400 μL of binding buffer was added to wash out excessive dyes. Samples were analyzed by flow cytometry within 1 h of staining.

4.12. Transwell migration assay

To utilize conditioned media from engineered MSCs, MSCs were seeded on 6-well plates at a density of 1.0×10^6 cells per well. Following 12 h of incubation, the culture medium was replaced with serum-free T cell medium (T cell culture medium without FBS). At 48 h, conditioned media were harvested, and 600 μL was placed in the bottom chamber of 12-well plates. Activated T cells (0.8×10^6) were resuspended in 200 μL T cell medium and seeded in 5 μm pore transwells (Corning, Corning, NY, USA; CLS3421). In parallel, serum-free T cell medium alone or supplemented with 1 μg/mL IP10-Fc fusion protein was used as controls. Upon 6 h incubation at 37°C, upper chambers were removed, and T cells that migrated to the bottom chamber were harvested and counted using a hemocytometer.

4.13. Intracellular cytokine analysis

For intracellular cytokine analysis, T cells were first treated with eBioscience protein transport inhibitor cocktail (Thermo Fisher Scientific; 00–4980–93) to prevent cytokine secretion. Cells were harvested after 6 h incubation. Fixation and permeabilization were then performed using the True-Nuclear Transcription Factor Buffer Set (BioLegend; 424401). After permeabilization step, cells were stained with fluorescence-labelled antibodies against IFNγ, TNFα, Granzyme B (detailed in Supplementary Table 1) in permeabilization buffer for 30 min at room temperature in the dark. Stained cells were washed and analyzed by flow cytometry.

4.14. In vivo tumor model and adoptive transfer of OT-I $CD8^+$ T cells

Tumor models were established by subcutaneous injection of cancer

cells into the shaved right flank of C57BL/6 N mice. For the MC38 model, each mouse was inoculated subcutaneously with 1.0×10^6 cells in 50 μL ice-cold DPBS. B16F10 and B16-OVA models were established similarly using 0.5×10^6 cells per mouse. CT26 models were established to BALB/c mice similarly using 1.0×10^6 cells per mouse. For immune subset depletion analysis, anti-CD8 (53–5.8), anti-CD4 (GK1.5) and anti-NK1.1 (PK136) obtained from BioXCell were i.p. injected twice a week for two weeks, starting the day before MSC injection. Tumor volumes were monitored every 3 days using calipers and calculated using the formula: volume = (length × width × depth)/2. MSCs were peritumorally injected when the tumor volume reached 100 mm^3. 1.5×10^6 NIP-MSCs were resuspended in 50 μL of ice-cold DPBS for injection.

For adoptive cell transfer, lymphodepletion was performed by intraperitoneal injection of 200 μL of cyclophosphamide solution (20 mg/mL; Sigma-Aldrich; C7397) one day before the MSC injection [61,62]. Two days after the lymphodepletion, 1.0×10^7 CFSE-labelled T cells or 1.0×10^6 OT-I $CD8^+$ T cells were adoptively transferred into B16 or B16-OVA tumor-bearing C57BL/6NCrlOri mice, respectively. All T cells were *in vitro* activated for 48 h before the adoptive transfer. Mice with tumor volumes exceeding 2000 mm^3 were considered to have reached the experimental endpoint.

4.15. Tissue dissociation and single-cell preparation

Peripheral blood was harvested using heparinized capillary tubes (Kimble Chase, Vineland, NJ, USA; 2501). Tumor and lung tissues were cut into small pieces and digested with collagenase A (1 mg/mL; Roche, Basel, Switzerland; COLLA-RO) and DNase I (0.5 mg/mL; Sigma-Aldrich; 10104159001) at 37°C for 45 min before being filtered through 70 μm cell strainers (Corning; 352350). Other harvested organs were directly filtered through 70 μm cell strainers. When necessary, red blood cell lysis was performed using 1 × RBC lysis buffer prepared by diluting eBioscience 10 × RBC lysis buffer (Thermo Fisher Scientific; 00–4300–54) in sterile distilled water. Single-cell suspensions were washed twice with DPBS supplemented with 2 % FBS and 0.5 mM EDTA (Thermo Fisher Scientific; 15575–038).

4.16. Tumor and tissue-infiltrating lymphocyte analysis

The single-cell suspensions were then incubated with anti-FcgIII/II receptor from clone 2.4G2 for 15 min, followed by surface marker staining using conjugated antibodies (Detailed information is listed on the Supplementary Table 1). Stained Samples were then washed twice with DPBS supplemented by 2 % FBS and 0.5 mM EDTA for flow cytometric analysis. Tumor-bearing mice with peritumorally injected the identical number of BM-MSC or without any injection were regarded as control. T cell detection was performed by identifying cells that were both $CD45^+$ and $CD3^+$ using fluorescence-conjugated antibodies (detailed in Supplementary Table 1). Adoptively transferred T cells were determined by detecting $V\alpha2^+$ T cells or $CFSE^+$ T cells.

4.17. MSC persistence & homing assay

To standardize tumor burden at the time of treatment, MSCs were injected when the average tumor volume reached 100 mm^3 . At this time point, NIP-MSCs were fluorescently labeled with 1 μM CFSE (Thermo Fisher Scientific; C34554), and 1.5×10^6 cells in 50 μL ice-cold DPBS were injected peritumorally into each tumor-bearing mouse, with BM-MSCs used as controls. Three days post-injection, tissues were harvested and processed into single-cell suspensions for flow cytometric analysis. MSC detection was performed by identifying cells that were both $CFSE^+$ and positive for MSCs-specific markers using fluorescence-conjugated antibodies (detailed in Supplementary Table 1).

4.18. In vivo IP10-Fc distribution analysis

1.5×10^6 cells of NIP-MSCs or BM-MSCs were injected into each tumor-bearing mouse as described above. 50 μL of 200 μg/mL IP10-Fc solution were injected intratumorally and considered as controls. Three days post-injection, tissues were harvested and processed into homogenates using FastPrep-24™ Homogenizer (MP Biomedicals, Santa Ana, CA, USA). 1 μM of phenylmethylsulfonyl fluoride (Sigma-Aldrich; P7626) and 1 × protease inhibitor cocktail prepared by diluting 100 × protease inhibitor cocktail (Seleckchem, Houston, TX, USA; B140002) were diluted in DPBS and used as homogenizing buffer. Homogenates have been centrifuged (16000 g for 10 min at 4 ℃) and the supernatents were harvested for ELISA analysis.

4.19. Statistical analysis

The number of animals and replicates are indicated in each figure legend. For *in vitro* experiments, wells were randomly assigned into each group and all cells were analyzed equally. For *in vivo* experiments, animals were distributed into groups using stratified randomization by tumor volume. All data were analyzed using GraphPad Prism 10 and shown as mean ±standard error of the mean (s.e.m.). *P* value was determined by two-way analysis of variance (ANOVA) for tumor growth, one-way ANOVA for TIL assay for MC38 model, B16-OVA ACT model, T cell bioinfiltration assay. Log-rank test for survival, unpaired two-tailed *t*-tests for the other analysis were used to determine the *P* value. ANOVA tests were followed by Holm-Šídák post-hoc test for comparisons involving more than two groups. All reported p-values were two-sided and were considered statistically significant at $^*P < 0.05$, $^{**}P < 0.01$, $^{***}P < 0.001$, and $^{****}P < 0.0001$.

CRediT authorship contribution statement

Jeong Ho Yoon: Writing – original draft, Validation, Methodology, Investigation, Formal analysis. **Joonbeom Bae:** Writing – original draft, Project administration, Funding acquisition, Conceptualization. **Yang-Xin Fu:** Writing – review & editing, Conceptualization. **Taehoon Chun:** Writing – review & editing, Resources. **Ji Hyung Kim:** Resources. **Dae-Sung Kim:** Resources, Methodology. **In-Byung Park:** Methodology. **Soo Seok Hwang:** Resources, Methodology. **Seok-Jin Kang:** Methodology. **Seon Ah Lim:** Resources, Methodology, Writing – review & editing. **Jiwon Oh:** Validation, Investigation, Formal analysis. **Gyu-Bum Yeon:** Writing – original draft, Validation, Methodology, Investigation, Formal analysis. **Hyunseo An:** Validation, Investigation, Formal analysis. **Hojae Lee:** Validation, Methodology, Investigation.

Declaration of Generative AI and AI-assisted technologies in the writing process

During the preparation of this work, the authors used Claude Sonnet 4 (Anthropic) in order to improve the readability, clarity and grammar of the manuscript. After using this tool, the authors reviewed and edited the content as needed and take full responsibility for the content of the published article.

Declaration of Competing Interest

The authors have declared that no conflict of interest exists.

Acknowledgments

This work was supported by a Korea University Grant and Basic Science Research Program through the National Research Foundation of Korea (NRF) grant funded by the Korea government (MSIT) (RS-2024–00398456, RS-2023–00244107, and RS-2024–00347015; J.B.). We thank BioRender for its use in creating schematic illustrations and

graphical abstract (https://BioRender.com/y9yvwhl). We thank the Institutional Animal Care and Use Committee Animal Resources Center, and Animal Research Center.

Appendix A. Supporting information

Supplementary data associated with this article can be found in the online version at doi:10.1016/j.biopha.2025.118579.

Data availability

Data will be made available on request. All data associated with this study are present in the paper or the Supplementary Materials. Requests for materials should be directed to the corresponding authors at joonbeombae@korea.ac.kr.

References

[1] S. Tan, D. Li, X. Zhu, Cancer immunotherapy: pros, cons and beyond, Biomed. Pharm. 124 (2020) 109821, https://doi.org/10.1016/j.biopha.2020.109821.
[2] H. Raskov, A. Orhan, J.P. Christensen, I. Gogenur, Cytotoxic CD8(+) t cells in cancer and cancer immunotherapy, Br. J. Cancer 124 (2) (2021) 359–367, https://doi.org/10.1038/s41416-020-01048-4.
[3] I. Melero, A. Rouzaut, G.T. Motz, G. Coukos, T-cell and NK-cell infiltration into solid tumors: a key limiting factor for efficacious cancer immunotherapy, Cancer Discov. 4 (5) (2014) 522–526, https://doi.org/10.1158/2159-8290.CD-13-0985.
[4] A.J. Gentles, A.M. Newman, C.L. Liu, S.V. Bratman, W. Feng, D. Kim, V.S. Nair, Y. Xu, A. Khuong, C.D. Hoang, M. Diehn, R.B. West, S.K. Plevritis, A.A. Alizadeh, The prognostic landscape of genes and infiltrating immune cells across human cancers, Nat. Med 21 (8) (2015) 938–945, https://doi.org/10.1038/nm.3909.
[5] P.C. Tumeh, C.L. Harview, J.H. Yearley, I.P. Shintaku, E.J. Taylor, L. Robert, B. Chmielowski, M. Spasic, G. Henry, V. Ciobanu, A.N. West, M. Carmona, C. Kivork, E. Seja, G. Cherry, A.J. Gutierrez, T.R. Grogan, C. Mateus, G. Tomasic, J. A. Glaspy, R.O. Emerson, H. Robins, R.H. Pierce, D.A. Elashoff, C. Robert, A. Ribas, PD-1 blockade induces responses by inhibiting adaptive immune resistance, Nature 515 (7528) (2014) 568–571, https://doi.org/10.1038/nature13954.
[6] M. Yi, T. Li, M. Niu, H. Zhang, Y. Wu, K. Wu, Z. Dai, Targeting cytokine and chemokine signaling pathways for cancer therapy, Signal Transduct. Target Ther. 9 (1) (2024) 176, https://doi.org/10.1038/s41392-024-01868-3.
[7] M.E. Mikucki, D.T. Fisher, J. Matsuzaki, J.J. Skitzki, N.B. Gaulin, J.B. Muhitch, A. W. Ku, J.G. Frelinger, K. Odunsi, T.F. Gajewski, A.D. Luster, S.S. Evans, Non-redundant requirement for CXCR3 signalling during tumoricidal T-cell trafficking across tumour vascular checkpoints, Nat. Commun. 6 (2015) 7458, https://doi.org/10.1038/ncomms8458.
[8] M. Metzemaekers, V. Vanheule, R. Janssens, S. Struyf, P. Proost, Overview of the mechanisms that May contribute to the Non-Redundant activities of Interferon-Inducible CXC chemokine receptor 3 ligands, Front Immunol. 8 (2017) 1970, https://doi.org/10.3389/fimmu.2017.01970.
[9] J. Flier, D.M. Boorsma, D.P. Bruynzeel, P.J. Van Beek, T.J. Stoof, R.J. Scheper, R. Willemze, C.P. Tensen, The CXCR3 activating chemokines IP-10, mig, and IP-9 are expressed in allergic but not in irritant patch test reactions, J. Invest Dermatol. 113 (4) (1999) 574–578, https://doi.org/10.1046/j.1523-1747.1999.00730.x.
[10] L. Lasagni, M. Francalanci, F. Annunziato, E. Lazzeri, S. Giannini, L. Cosmi, C. Sagrinati, B. Mazzinghi, C. Orlando, E. Maggi, F. Marra, S. Romagnani, M. Serio, P. Romagnani, An alternatively spliced variant of CXCR3 mediates the inhibition of endothelial cell growth induced by IP-10, mig, and I-TAC, and acts as functional receptor for platelet factor 4, J. Exp. Med 197 (11) (2003) 1537–1549, https://doi.org/10.1084/jem.20021897.
[11] F. Sierro, C. Biben, L. Martinez-Munoz, M. Mellado, R.M. Ransohoff, M. Li, B. Woehl, H. Leung, J. Groom, M. Batten, R.P. Harvey, A.C. Martinez, C.R. Mackay, F. Mackay, Disrupted cardiac development but normal hematopoiesis in mice deficient in the second CXCL12/SDF-1 receptor, CXCR7, Proc. Natl. Acad. Sci. 104 (37) (2007) 14759–14764, https://doi.org/10.1073/pnas.0702229104.
[12] M. Muller, S. Carter, M.J. Hofer, I.L. Campbell, Review: the chemokine receptor CXCR3 and its ligands CXCL9, CXCL10 and CXCL11 in neuroimmunity–a tale of conflict and conundrum, Neuropathol. Appl. Neurobiol. 36 (5) (2010) 368–387, https://doi.org/10.1111/j.1365-2990.2010.01089.x.
[13] Y. Yuan, J. Xu, G. Chen, Y. Liu, L. Ouyang, B. Ma, B. Wang, W. Yan, Q. Zhang, Q. Ma, J. Zhang, X. Mao, X. Zhang, Y. Geng, H. Wang, Y. Li, P. Zheng, R. Wang, Comparable immune escape capacity between KP.2 and other SARS-CoV-2 variants in the central Chinese population after the first COVID-19 booster, Sci. Rep. 15 (1) (2025) 17762, https://doi.org/10.1038/s41598-025-02927-7.
[14] X. Wang, X.L. Lu, H.Y. Zhao, F.C. Zhang, X.B. Jiang, A novel recombinant protein of IP10-EGFRvIIIscFv and CD8(+) cytotoxic t lymphocytes synergistically inhibits the growth of implanted glioma in mice, 72, Cancer Immunol. Immunother. 62 (7) (2013) 1261, https://doi.org/10.1007/s00262-013-1426-6.
[15] U. Barash, Y. Zohar, G. Wildbaum, K. Beider, A. Nagler, N. Karin, N. Ilan, I. Vlodavsky, Heparanase enhances myeloma progression via CXCL10 downregulation, 87, Leukemia 28 (11) (2014) 2178, https://doi.org/10.1038/leu.2014.121.
[16] C.M. Van Herpen, R. Huijbens, M. Looman, J. De Vries, H. Marres, J. Van De Ven, R. Hermsen, G.J. Adema, P.H. De Mulder, Pharmacokinetics and immunological aspects of a phase ib study with intratumoral administration of recombinant human interleukin-12 in patients with head and neck squamous cell carcinoma: a decrease of T-bet in peripheral blood mononuclear cells, Clin. Cancer Res 9 (8) (2003) 2950, 6.
[17] N. Momin, N.K. Mehta, N.R. Bennett, L. Ma, J.R. Palmeri, M.M. Chinn, E.A. Lutz, B. Kang, D.J. Irvine, S. Spranger, K.D. Wittrup, Anchoring of intratumorally administered cytokines to collagen safely potentiates systemic cancer immunotherapy, Sci. Transl. Med 11 (498) (2019), https://doi.org/10.1126/scitranslmed.aaw2614.
[18] C. Owen-Woods, R. Joulia, A. Barkaway, L. Rolas, B. Ma, A.F. Nottebaum, K. P. Arkill, M. Stein, T. Girbl, M. Golding, D.O. Bates, D. Vestweber, M.B. Voisin, S. Nourshargh, Local microvascular leakage promotes trafficking of activated neutrophils to remote organs, J. Clin. Invest 130 (5) (2020) 2301–2318, https://doi.org/10.1172/JCI133661.
[19] H. Sun, W. Yao, D. Cheng, H. Chen, X. Du, G. Hou, Monitoring Early-Stage acute rejection by imaging CXCR3-Positive cell infiltration: evaluation of (1)(2)(5) Iodine-Labeled CXCL10, Exp. Clin. Transpl. 18 (3) (2020) 368–374, https://doi.org/10.6002/ect.2019.0346.
[20] R. Barreira da Silva, M.E. Laird, N. Yatim, L. Fiette, M.A. Ingersoll, M.L. Albert, Dipeptidylpeptidase 4 inhibition enhances lymphocyte trafficking, improving both naturally occurring tumor immunity and immunotherapy, 8, Nat. Immunol. 16 (8) (2015) 850, https://doi.org/10.1038/ni.3201.
[21] N. Pang, J. Shi, L. Qin, A. Chen, Y. Tang, H. Yang, Y. Huang, Q. Wu, X. Li, B. He, T. Li, B. Liang, J. Zhang, B. Cao, M. Liu, Y. Feng, X. Ye, X. Chen, L. Wang, Y. Tian, H. Li, J. Li, H. Hu, J. He, Y. Hu, C. Zhi, Z. Tang, Y. Gong, F. Xu, L. Xu, W. Fan, M. Zhao, D. Chen, H. Lian, L. Yang, P. Li, Z. Zhang, IL-7 and CCL19-secreting CAR-T cell therapy for tumors with positive glypican-3 or mesothelin, J. Hematol. Oncol. 14 (1) (2021) 118, https://doi.org/10.1186/s13045-021-01128-9.
[22] S. Nie, Y. Song, K. Hu, W. Zu, F. Zhang, L. Chen, Q. Ma, Z. Zhou, S. Jiao, CXCL10 and IL15 co-expressing chimeric antigen receptor t cells enhance anti-tumor effects in gastric cancer by increasing cytotoxic effector cell accumulation and survival, Oncoimmunology 13 (1) (2024) 2358590, https://doi.org/10.1080/2162402X.2024.2358590.
[23] M. Studeny, F.C. Marini, J.L. Dembinski, C. Zompetta, M. Cabreira-Hansen, B. N. Bekele, R.E. Champlin, M. Andreeff, Mesenchymal stem cells: potential precursors for tumor stroma and targeted-delivery vehicles for anticancer agents, 603, J. Natl. Cancer Inst. 96 (21) (2004) 1593, https://doi.org/10.1093/jnci/djh299.
[24] S. Komarova, Y. Kawakami, M.A. Stoff-Khalili, D.T. Curiel, L. Pereboeva, Mesenchymal progenitor cells as cellular vehicles for delivery of oncolytic adenoviruses, 66, Mol. Cancer Ther. 5 (3) (2006) 755, https://doi.org/10.1158/1535-7163.MCT-05-0334.
[25] K. Lee, M.K. Majumdar, D. Buyaner, J.K. Hendricks, M.F. Pittenger, J.D. Mosca, Human mesenchymal stem cells maintain transgene expression during expansion and differentiation, 66, Mol. Ther. 3 (6) (2001) 857, https://doi.org/10.1006/mthe.2001.0327.
[26] K. Ozawa, K. Sato, I. Oh, K. Ozaki, R. Uchibori, Y. Obara, Y. Kikuchi, T. Ito, T. Okada, M. Urabe, H. Mizukami, A. Kume, Cell and gene therapy using mesenchymal stem cells (MSCs), 7, J. Autoimmun. 30 (3) (2008) 121, https://doi.org/10.1016/j.jaut.2007.12.008.
[27] Y. Wang, H. Yi, Y. Song, The safety of MSC therapy over the past 15 years: a meta-analysis, Stem Cell Res Ther. 12 (1) (2021) 545, https://doi.org/10.1186/s13287-021-02609-x.
[28] Y. Shi, J. Zhang, Y. Li, C. Feng, C. Shao, Y. Shi, J. Fang, Engineered mesenchymal stem/stromal cells against cancer, Cell Death Dis. 16 (1) (2025) 113, https://doi.org/10.1038/s41419-025-07443-0.
[29] N. Kulach, E. Pilny, T. Cichon, J. Czapla, M. Jarosz-Biej, M. Rusin, A. Drzyzga, S. Matuszczak, S. Szala, R. Smolarczyk, Mesenchymal stromal cells as carriers of IL-12 reduce primary and metastatic tumors of murine melanoma, Sci. Rep. 11 (1) (2021) 18335, https://doi.org/10.1038/s41598-021-97435-9.
[30] M.K. McKenna, A. Englisch, B. Brenner, T. Smith, V. Hoyos, M. Suzuki, M. K. Brenner, Mesenchymal stromal cell delivery of oncolytic immunotherapy improves CAR-T cell antitumor activity, Mol. Ther. 29 (5) (2021) 1808–1820, https://doi.org/10.1016/j.ymthe.2021.02.004.
[31] A. Moya, J. Paquet, M. Deschepper, N. Larochette, K. Oudina, C. Denoeud, M. Bensidhoum, D. Logeart-Avramoglou, H. Petite, Human mesenchymal stem cell failure to adapt to glucose shortage and rapidly use intracellular energy reserves through glycolysis explains poor cell survival after implantation, 376, Stem Cells 36 (3) (2018) 363, https://doi.org/10.1002/stem.2763.
[32] A.H. Nwabo Kamdje, P.F. Seke Etet, R. Simo Tagne, L. Vecchio, K.E. Lukong, M. Krampera, Tumor microenvironment uses a reversible reprogramming of mesenchymal stromal cells to mediate Pro-tumorigenic effects, Front Cell Dev. Biol. 8 (2020) 545126, https://doi.org/10.3389/fcell.2020.545126.
[33] D. Ross, D. Siegel, The diverse functionality of NQO1 and its roles in redox control, Redox Biol. 41 (2021) 101950, https://doi.org/10.1016/j.redox.2021.101950.
[34] P.L. Chesis, D.E. Levin, M.T. Smith, L. Ernster, B.N. Ames, Mutagenicity of quinones: pathways of metabolic activation and detoxification, 700, Proc. Natl. Acad. Sci. USA 81 (6) (1984) 1696, https://doi.org/10.1073/pnas.81.6.1696.
[35] D. Siegel, C. Yan, D. Ross, NAD(P)H:quinone oxidoreductase 1 (NQO1) in the sensitivity and resistance to antitumor quinones, 40, Biochem Pharm. 83 (8) (2012) 1033, https://doi.org/10.1016/j.bcp.2011.12.017.
[36] E.T. Oh, J.W. Kim, J.M. Kim, S.J. Kim, J.S. Lee, S.S. Hong, J. Goodwin, R. J. Ruthenborg, M.G. Jung, H.J. Lee, C.H. Lee, E.S. Park, C. Kim, H.J. Park, NQO1

inhibits proteasome-mediated degradation of HIF-1alpha, Nat. Commun. 7 (2016) 13593, https://doi.org/10.1038/ncomms13593.
[37] D.H. Hyun, J. Kim, C. Moon, C.J. Lim, R. de Cabo, M.P. Mattson, The plasma membrane redox enzyme NQO1 sustains cellular energetics and protects human neuroblastoma cells against metabolic and proteotoxic stress, 70, Age (Dordr.) 34 (2) (2012) 359, https://doi.org/10.1007/s11357-011-9245-1.
[38] T. Li, J. Fu, Z. Zeng, D. Cohen, J. Li, Q. Chen, B. Li, X.S. Liu, TIMER2.0 for analysis of tumor-infiltrating immune cells, Nucleic Acids Res. 48 (W1) (2020) W509–W514, https://doi.org/10.1093/nar/gkaa407.
[39] L.A. Turka, P.S. Linsley, H. Lin, W. Brady, J.M. Leiden, R.Q. Wei, M.L. Gibson, X. G. Zheng, S. Myrdal, D. Gordon, et al., T-cell activation by the CD28 ligand B7 is required for cardiac allograft rejection in vivo, 5, Proc. Natl. Acad. Sci. USA 89 (22) (1992) 11102, https://doi.org/10.1073/pnas.89.22.11102.
[40] J.R. Abrams, M.G. Lebwohl, C.A. Guzzo, B.V. Jegasothy, M.T. Goldfarb, B.S. Goffe, A. Menter, N.J. Lowe, G. Krueger, M.J. Brown, R.S. Weiner, M.J. Birkhofer, G. L. Warner, K.K. Berry, P.S. Linsley, J.G. Krueger, H.D. Ochs, S.L. Kelley, S. Kang, CTLA4Ig-mediated blockade of T-cell costimulation in patients with psoriasis vulgaris, 52, J. Clin. Invest 103 (9) (1999) 1243, https://doi.org/10.1172/JCI5857.
[41] Y. Wang, D.J. Irvine, Engineering chemoattractant gradients using chemokine-releasing polysaccharide microspheres, 13, Biomaterials 32 (21) (2011) 4903, https://doi.org/10.1016/j.biomaterials.2011.03.027.
[42] D. Qiu, S. Song, Y. Wang, Y. Bian, M. Wu, H. Wu, Y. Shi, H. Duan, NAD(P)H: quinone oxidoreductase 1 attenuates oxidative stress and apoptosis by regulating Sirt1 in diabetic nephropathy, J. Transl. Med 20 (1) (2022) 44, https://doi.org/10.1186/s12967-021-03197-3.
[43] H.S. Jo, D.S. Kim, E.H. Ahn, D.W. Kim, M.J. Shin, S.B. Cho, J.H. Park, C.H. Lee, E. J. Yeo, Y.J. Choi, H.J. Yeo, C.S. Chung, S.W. Cho, K.H. Han, J. Park, W.S. Eum, S. Y. Choi, Protective effects of Tat-NQO1 against oxidative stress-induced HT-22 cell damage, and ischemic injury in animals, BMB Rep. 49 (11) (2016) 617–622, https://doi.org/10.5483/bmbrep.2016.49.11.117.
[44] A. Shen, H.J. Kim, G.S. Oh, S.B. Lee, S. Lee, A. Pandit, D. Khadka, S. Sharma, S. Y. Kim, S.K. Choe, S.H. Yang, E.Y. Cho, H. Shim, R. Park, T.H. Kwak, H.S. So, Pharmacological stimulation of NQO1 decreases NADPH levels and ameliorates acute pancreatitis in mice, Cell Death Dis. 10 (1) (2018) 5, https://doi.org/10.1038/s41419-018-1252-z.
[45] A.S. Divakaruni, M. Jastroch, A practical guide for the analysis, standardization and interpretation of oxygen consumption measurements, Nat. Metab. 4 (8) (2022) 978–994, https://doi.org/10.1038/s42255-022-00619-4.
[46] J. Michl, K.C. Park, P. Swietach, Evidence-based guidelines for controlling ph in mammalian live-cell culture systems, Commun. Biol. 2 (2019) 144, https://doi.org/10.1038/s42003-019-0393-7.
[47] W. Li, G. Ren, Y. Huang, J. Su, Y. Han, J. Li, X. Chen, K. Cao, Q. Chen, P. Shou, L. Zhang, Z.R. Yuan, A.I. Roberts, S. Shi, A.D. Le, Y. Shi, Mesenchymal stem cells: a double-edged sword in regulating immune responses, 13, Cell Death Differ. 19 (9) (2012) 1505, https://doi.org/10.1038/cdd.2012.26.
[48] C. Moore, J. Bae, L. Liu, H. Li, Y.X. Fu, J. Qiao, Exogenous signaling repairs defective t cell signaling inside the tumor microenvironment for better immunity, JCI Insight 7 (17) (2022), https://doi.org/10.1172/jci.insight.159479.
[49] J. Bae, L. Liu, C. Moore, E. Hsu, A. Zhang, Z. Ren, Z. Sun, X. Wang, J. Zhu, J. Shen, J. Qiao, Y.X. Fu, IL-2 delivery by engineered mesenchymal stem cells re-invigorates CD8(+) t cells to overcome immunotherapy resistance in cancer, Nat. Cell Biol. 24 (12) (2022) 1754–1765, https://doi.org/10.1038/s41556-022-01024-5.
[50] N. Wakabayashi-Ito, S. Nagata, Characterization of the regulatory elements in the promoter of the human elongation factor-1 alpha gene, J. Biol. Chem. 269 (47) (1994) 29831, 7.
[51] A. Gros, P.F. Robbins, X. Yao, Y.F. Li, S. Turcotte, E. Tran, J.R. Wunderlich, A. Mixon, S. Farid, M.E. Dudley, K. Hanada, J.R. Almeida, S. Darko, D.C. Douek, J. C. Yang, S.A. Rosenberg, PD-1 identifies the patient-specific CD8(+) tumor-reactive repertoire infiltrating human tumors, 59, J. Clin. Invest 124 (5) (2014) 2246, https://doi.org/10.1172/JCI73639.
[52] D.S. Thommen, V.H. Koelzer, P. Herzig, A. Roller, M. Trefny, S. Dimeloe, A. Kiialainen, J. Hanhart, C. Schill, C. Hess, S. Savic Prince, M. Wiese, D. Lardinois, P.C. Ho, C. Klein, V. Karanikas, K.D. Mertz, T.N. Schumacher, A. Zippelius, A transcriptionally and functionally distinct PD-1(+) CD8(+) t cell pool with predictive potential in non-small-cell lung cancer treated with PD-1 blockade, Nat. Med 24 (7) (2018) 994–1004, https://doi.org/10.1038/s41591-018-0057-z.
[53] R. Yang, L. Sun, C.F. Li, Y.H. Wang, J. Yao, H. Li, M. Yan, W.C. Chang, J.M. Hsu, J. H. Cha, J.L. Hsu, C.W. Chou, X. Sun, Y. Deng, C.K. Chou, D. Yu, M.C. Hung, Galectin-9 interacts with PD-1 and TIM-3 to regulate t cell death and is a target for cancer immunotherapy, Nat. Commun. 12 (1) (2021) 832, https://doi.org/10.1038/s41467-021-21099-2.
[54] M. Roussel, K.S. Le, C. Granier, F. Llamas Gutierrez, E. Foucher, S. Le Gallou, C. Pangault, L. Xerri, V. Launay, T. Lamy, E. Tartour, D. Olive, T. Fest, Functional characterization of PD1+TIM3+ tumor-infiltrating t cells in DLBCL and effects of PD1 or TIM3 blockade, Blood Adv. 5 (7) (2021) 1816–1829, https://doi.org/10.1182/bloodadvances.2020003080.
[55] S.A. Minnie, O.G. Waltner, P. Zhang, S. Takahashi, N.S. Nemychenkov, K. S. Ensbey, C.R. Schmidt, S.R.W. Legg, M. Comstock, J.R. Boiko, E. Nelson, S. S. Bhise, A.B. Wilkens, M. Koyama, M.V. Dhodapkar, M. Chesi, S.R. Riddell, D. J. Green, A. Spencer, S.N. Furlan, G.R. Hill, TIM-3(+) CD8 t cells with a terminally exhausted phenotype retain functional capacity in hematological malignancies, Sci. Immunol. 9 (94) (2024) eadg1094, https://doi.org/10.1126/sciimmunol.adg1094.
[56] R. Tokunaga, W. Zhang, M. Naseem, A. Puccini, M.D. Berger, S. Soni, M. McSkane, H. Baba, H.J. Lenz, CXCL9, CXCL10, CXCL11/CXCR3 axis for immune activation - a target for novel cancer therapy, Cancer Treat. Rev. 63 (2018) 40–47, https://doi.org/10.1016/j.ctrv.2017.11.007.
[57] M.T. Chow, A.J. Ozga, R.L. Servis, D.T. Frederick, J.A. Lo, D.E. Fisher, G. J. Freeman, G.M. Boland, A.D. Luster, Intratumoral activity of the CXCR3 chemokine system is required for the efficacy of Anti-PD-1 therapy, e5, Immunity 50 (6) (2019) 1498–1512, https://doi.org/10.1016/j.immuni.2019.04.010.
[58] N. Abdala-Saleh, J. Lugassy, A. Shivakumar-Kalvhati, A. Turky, S. Abu Ras, H. Razon, N. Berger, D. Bar-On, Y. Bar-On, T. Taura, D. Wilson, N. Karin, PD-1 and CTLA-4 serve as major gatekeepers for effector and cytotoxic T-cell potentiation by limiting a CXCL9/10-CXCR3-IFNgamma positive feedback loop, Front Immunol. 15 (2024) 1452212, https://doi.org/10.3389/fimmu.2024.1452212.
[59] I.G. House, P. Savas, J. Lai, A.X.Y. Chen, A.J. Oliver, Z.L. Teo, K.L. Todd, M. A. Henderson, L. Giuffrida, E.V. Petley, K. Sek, S. Mardiana, T.N. Gide, C. Quek, R. A. Scolyer, G.V. Long, J.S. Wilmott, S. Loi, P.K. Darcy, P.A. Beavis, Macrophage-Derived CXCL9 and CXCL10 are required for antitumor immune responses following immune checkpoint blockade, Clin. Cancer Res 26 (2) (2020) 487–504, https://doi.org/10.1158/1078-0432.CCR-19-1868.
[60] Z. Shi, J. Shen, J. Qiu, Q. Zhao, K. Hua, H. Wang, CXCL10 potentiates immune checkpoint blockade therapy in homologous recombination-deficient tumors, Theranostics 11 (15) (2021) 7175–7187, https://doi.org/10.7150/thno.59056.
[61] T. Yin, G. Wang, L. Wang, P. Mudgal, E. Wang, C.C. Pan, P.B. Alexander, H. Wu, C. Cao, Y. Liang, L. Tan, D. Huang, M. Chong, R. Chen, B.J.W. Lim, K. Xiang, W. Xue, L. Wan, H. Hu, Y.H. Loh, X.F. Wang, Q.J. Li, Breaking NGF-TrkA immunosuppression in melanoma sensitizes immunotherapy for durable memory t cell protection, Nat. Immunol. 25 (2) (2024) 268–281, https://doi.org/10.1038/s41590-023-01723-7.
[62] L. Tan, T. Yin, H. Xiang, L. Wang, P. Mudgal, J. Chen, Y. Ding, G. Wang, B.J. W. Lim, Y. Huang, D. Huang, Y. Liang, P.B. Alexander, K. Xiang, E. Wang, C. Yan, Z. Ma, M. Tan, Q.J. Li, X.F. Wang, Aberrant cytoplasmic expression of UHRF1 restrains the MHC-I-mediated anti-tumor immune response, Nat. Commun. 15 (1) (2024) 8569, https://doi.org/10.1038/s41467-024-52902-5.
[63] J. Foeng, I. Comerford, S.R. McColl, Harnessing the chemokine system to home CAR-T cells into solid tumors, Cell Rep. Med 3 (3) (2022) 100543, https://doi.org/10.1016/j.xcrm.2022.100543.
[64] M.M. Wang, S.E. Coupland, T. Aittokallio, C.R. Figueiredo, Resistance to immune checkpoint therapies by tumour-induced T-cell desertification and exclusion: key mechanisms, prognostication and new therapeutic opportunities, Br. J. Cancer 129 (8) (2023) 1212–1224, https://doi.org/10.1038/s41416-023-02361-4.
[65] A.M. Lambeir, P. Proost, C. Durinx, G. Bal, K. Senten, K. Augustyns, S. Scharpe, J. Van Damme, I. De Meester, Kinetic investigation of chemokine truncation by CD26/dipeptidyl peptidase IV reveals a striking selectivity within the chemokine family, 45, J. Biol. Chem. 276 (32) (2001) 29839, https://doi.org/10.1074/jbc.M103106200.
[66] R.J. Lim, R. Salehi-Rad, L.M. Tran, M.S. Oh, C. Dumitras, W.P. Crosson, R. Li, T. S. Patel, S. Man, C.E. Yean, J. Abascal, Z. Huang, S.L. Ong, K. Krysan, S. M. Dubinett, B. Liu, CXCL9/10-engineered dendritic cells promote t cell activation and enhance immune checkpoint blockade for lung cancer, Cell Rep. Med 5 (4) (2024) 101479, https://doi.org/10.1016/j.xcrm.2024.101479.
[67] J. Mao, J. Li, J. Chen, Q. Wen, M. Cao, F. Zhang, B. Li, Q. Zhang, Z. Wang, J. Zhang, J. Shen, CXCL10 and Nrf2-upregulated mesenchymal stem cells reinvigorate t lymphocytes for combating glioblastoma, J. Immunother. Cancer 11 (12) (2023), https://doi.org/10.1136/jitc-2023-007481.
[68] D. Jovic, Y. Yu, D. Wang, K. Wang, H. Li, F. Xu, C. Liu, J. Liu, Y. Luo, A brief overview of global trends in MSC-Based cell therapy, Stem Cell Rev. Rep. 18 (5) (2022) 1525–1545, https://doi.org/10.1007/s12015-022-10369-1.
[69] G. Vlahou, M. Elias, J.C. von Kleist-Retzow, R.J. Wiesner, F. Rivero, The ras related GTPase miro is not required for mitochondrial transport in dictyostelium discoideum, 55, Eur. J. Cell Biol. 90 (4) (2011) 342, https://doi.org/10.1016/j.ejcb.2010.10.012.
[70] T. Abdul-Rahman, S. Ghosh, S.M. Badar, A. Nazir, G.B. Bamigbade, N. Aji, P. Roy, H. Kachani, N. Garg, L. Lawal, Z.S.B. Bliss, A.A. Wireko, O. Atallah, F. T. Adebusoye, T. Teslyk, K. Sikora, V. Horbas, The paradoxical role of cytokines and chemokines at the tumor microenvironment: a comprehensive review, Eur. J. Med Res 29 (1) (2024) 124, https://doi.org/10.1186/s40001-024-01711-z.
[71] M. O'Hayre, C.L. Salanga, T.M. Handel, D.J. Hamel, Emerging concepts and approaches for chemokine-receptor drug discovery, 22, Expert Opin. Drug Discov. 5 (11) (2010) 1109, https://doi.org/10.1517/17460441.2010.525633.
[72] R. Cabrita, M. Lauss, A. Sanna, M. Donia, M. Skaarup Larsen, S. Mitra, I. Johansson, B. Phung, K. Harbst, J. Vallon-Christersson, A. van Schoiack, K. Lovgren, S. Warren, K. Jirstrom, H. Olsson, K. Pietras, C. Ingvar, K. Isaksson, D. Schadendorf, H. Schmidt, L. Bastholt, A. Carneiro, J.A. Wargo, I.M. Svane, G. Jonsson, Tertiary lymphoid structures improve immunotherapy and survival in melanoma, Nature 577 (7791) (2020) 561–565, https://doi.org/10.1038/s41586-019-1914-8.
[73] L. Vanhersecke, M. Brunet, J.P. Guegan, C. Rey, A. Bougouin, S. Cousin, S. L. Moulec, B. Besse, Y. Loriot, M. Larroquette, I. Soubeyran, M. Toulmonde, G. Roubaud, S. Pernot, M. Cabart, F. Chomy, C. Lefevre, K. Bourcier, M. Kind, I. Giglioli, C. Sautes-Fridman, V. Velasco, F. Courgeon, E. Oflazoglu, A. Savina, A. Marabelle, J.C. Soria, C. Bellera, C. Sofeu, A. Bessede, W.H. Fridman, F. L. Loarer, A. Italiano, Mature tertiary lymphoid structures predict immune

checkpoint inhibitor efficacy in solid tumors independently of PD-L1 expression, Nat. Cancer 2 (8) (2021) 794–802, https://doi.org/10.1038/s43018-021-00232-6.
[74] E.J. Hsu, X. Cao, B. Moon, J. Bae, Z. Sun, Z. Liu, Y.X. Fu, A cytokine receptor-masked IL2 prodrug selectively activates tumor-infiltrating lymphocytes for potent antitumor therapy, Nat. Commun. 12 (1) (2021) 2768, https://doi.org/10.1038/s41467-021-22980-w.
[75] J. Bae, S.P. Choi, K. Isono, J.Y. Lee, S.W. Park, C.Y. Choi, J. Han, S.H. Kim, H. H. Lee, K. Park, H.Y. Jin, S.J. Lee, C.G. Park, H. Koseki, Y.S. Lee, T. Chun, Phc2 controls hematopoietic stem and progenitor cell mobilization from bone marrow by repressing Vcam1 expression, Nat. Commun. 10 (1) (2019) 3496, https://doi.org/10.1038/s41467-019-11386-4.